POLARIZATION INCLUDED GEOMETRY BASED CHANNEL MODELING FOR MIMO SYSTEMS

A THESIS
SUBMITTED TO THE DEPARTMENT OF ELECTRICAL AND ELECTRONICS ENGINEERING
AND THE INSTITUTE OF ENGINEERING AND SCIENCE
OF BİLKENT UNIVERSITY
IN PARTIAL FULFILLMENT OF THE REQUIREMENTS
FOR THE DEGREE OF
MASTER OF SCIENCE

By

Keziban Akkaya

September 2008

I certify that I have read this thesis and that in my opinion it is fully adequate, in scope and in quality, as a thesis for the degree of Master of Science.

Prof. Dr. Ayhan Altıntaş(Supervisor)

I certify that I have read this thesis and that in my opinion it is fully adequate, in scope and in quality, as a thesis for the degree of Master of Science.

Assist. Prof. Dr. Defne Aktaş

I certify that I have read this thesis and that in my opinion it is fully adequate, in scope and in quality, as a thesis for the degree of Master of Science.

Prof. Dr. Birsen Saka Tanatar

Approved for the Institute of Engineering and Science:

Prof. Dr. Mehmet Baray
Director of Institute of Engineering and Science

ABSTRACT

POLARIZATION INCLUDED GEOMETRY BASED CHANNEL MODELING FOR MIMO SYSTEMS

Keziban Akkaya
M.S. in Electrical and Electronics Engineering
Supervisor: Prof. Dr. Ayhan Altıntaş
September 2008

Most of the studies in the literature about channel modeling do not include the polarization. Aiming to develop a more realistic geometric model including polarization, the channel characteristics are examined using measurement data. Each multipath in the measurement data is modeled with a scatterer. Locations of scatterers are determined in the geometry based single bounce model. Then, each scatterer is replaced by a thin impedance disc. Electrical properties, sizes and orientations of discs are obtained using physical optics approximation. Using the channel model, XPD characteristics of the environment are examined. As a result of this study, a channel model for characterizing the general scenarios as much as possible is developed.

Keywords: Multiple Input Multiple Output (MIMO), Channel Modeling , Polarization, Cross Polarization Discrimination (XPD), Physical Optics (PO), Ray Tracing

ÖZET

MIMO SİSTEMLER İÇİN POLARİZASYON İÇEREN GEOMETRİK KANAL MODELLEMESİ

Keziban Akkaya
Elektrik ve Elektronik Mühendisliği Bölümü Yüksek Lisans
Tez Yöneticisi: Prof. Dr. Ayhan Altıntaş
Eylül 2008

Literatürdeki kanal modellemesi çalışmalarının çoğu polarizasyon içermemektedir. Polarizasyon etkilerini içeren daha gerçekçi bir kanal modeli geliştirmek amacıyla, ölçüm sonuçları kullanılarak kanalın davranışı incelendi. Ölçümde yer alan her bir çoklu yol bir saçınım nesnesi olarak modellendi. Saçınım nesnelerinin yerleri hesaplandı ve bu nesneler ince empedans diskleriyle modellendi. Disklerin elektriksel özellikleri, boyutları ve yönlenmeleri fiziksel optik teorisi kullanarak elde edildi. Elde edilen kanal modeli kullanılarak ortamın karşı polarizasyon ayrışım özelliği incelendi. Bu çalışma sonunda genel senaryoların kanal özelliklerini mümkün olduğunca karakterize eden bir kanal modeli elde edilmiştir.

Anahtar Kelimeler: Çok Girişli Çok Çıkışlı, Kanal Modelleme, Polarizasyon, Karşı Polarizasyon Ayrışımı, Fiziksel Optik, Işın İzleme Metodu

ACKNOWLEDGMENTS

I gratefully thank my supervisor Prof. Dr. Ayhan Altıntaş and Asst. Prof. Dr. Defne Aktaş for their suggestions, supervisions, and guidances throughout the development of this thesis.

I would also like to thank Prof. Dr. Birsen Saka Tanatar, the member of my jury, for reading and commenting on the thesis.

Finally, I am so thankful to my family for their support.

This thesis is partly supported by TUBITAK through the project EEEAG-106E081.

Contents

List of Figures

List of Tables

to my eternal beloved one...

Chapter 1

Introduction

Recently multiple input multiple output (MIMO) systems have drawn increasing attention in the literature due to increased channel performance and capacity. MIMO systems require the use of antenna arrays at both the receiver and the transmitter. Each receiver antenna collects all the signals propagating from multiple transmitter antennas. A schematic illustration of MIMO system is shown in Figure 1.1.

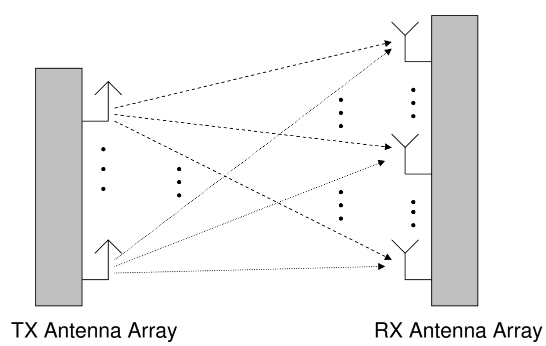

Figure 1.1: Schematic illustration of MIMO system

Since MIMO techniques are still under development, working on easy and meaningful methods for the modeling of MIMO channels has gained much importance [1]. Increasing number of antennas provides spatial diversity but on the other hand increases the spatial dimensions since there is a limitation on the separation between neighboring antennas. A number of spatial channel models are studied in the literature. For the systems with limited space, the use of dual polarized antennas is an effective alternative. But, only a limited number of polarization included channel models have been investigated. This is because coupling effect between orthogonal polarizations caused by scatterers is a complex process [2].

Using measurement results, [3] and [4] show that dual polarization systems improve channel performance compared to the single polarization systems. Also, in Ricean channels, dual polarized systems have better performance [5]. These improvements in system performance encourage people to work on polarization included channel modeling. Mainly these works are based on measurements and geometrical representation of the channel is not considered. A more accurate polarization included geometric channel model is an issue still being discussed. In [6], polarization characteristics of indoor ultrawide band channel are examined using channel measurements. In [7] and [8], electromagnetic scattering MIMO channel model is formulated using directional properties of several objects. Scatterings of cylinders and spheres are calculated separately by including amplitude and directional properties of propagating signals yielding long and complex calculations. A volumetric MIMO channel model is presented in [9]. It is a numerical approach for multipath scattering channels and channel consists of finite spatial volumes for transmitting and reception. In [2], a stochastic geometry-based MIMO scattering model is built using polarization matrices which are composed of random numbers whose distributions are obtained from measurements. In [10], polarization characteristics of the MIMO channel are investigated using polarization rotation angle between the transmitter and the receiver without a geometrical representation. In [11], a MIMO cross polarized channel is presented to examine the dependence of cross polarization discrimination on distance using measurements.

In this thesis, we propose a polarization included geometric channel model. For this purpose, measurement campaign carried by Elektrobit Testing Corporation is used. Measurement data consist of several scenarios and each indoor MIMO scenario includes particular number of multipaths. Using the measurement data, channel parameters are estimated for each multipath component (MPC) and each MPC is modeled as single bounce scatterer model. Hence, locations of scatterers are found using single bounce model estimation. After all scatterer locations are calculated, synthetic scenarios are constituted to decide on which multipaths can be represented with single bounce model. Electrical properties, shapes and orientations of the scatterers are obtained from scattering coefficients of these scatterers. These scatterers are modeled with discs and sizes of the discs are calculated using physical optics (PO). So, each scatterer is characterized physically and electrically. Hence, this channel model can be used to model any environment with all parameters determined accurately. It is a good tool to handle more complicated problems.

This thesis is arranged as follows. In Chapter 2, information about measurement campaign is given; in Chapter 3, the geometric MIMO channel model which includes polarization properties is described; in Chapter 4, this channel model is used to investigate the polarization properties of a scenario using cross polarization discrimination. The result is compared with ray tracing model and model presented in [11]. Finally, conclusion is drawn in Chapter 5.

Chapter 2

Measurement Campaign and Data

2.1 Introduction

This chapter describes the indoor measurement campaign carried out in June 2005 by Elektrobit Testing Corporation, Oulu, Finland [12]. The campaign consists of stationary spot measurements at 5 GHz frequency band using a Channel Sounder located on the 4th floor in Information Technology Department, in the main building of University of Oulu.

2.2 Environment and Measurement

The measurement site is a typical office environment with straight corridors and office rooms at both sides of the corridor. The building is made of concrete and steel. The room height is around 2.7m. Indoor walls are constructed of partly lightweight plaster and partly concrete. There are both line-of-sight (LOS) and non-line-of-sight (NLOS) scenarios.

There are 5 different scenario types shown below:

Table 2.1: List of measurement scenarios

	Scenario Type	Number of Measurements
1	Room-Corridor NLOS	6 Static Spots
2	Room-Room NLOS	1 Static Spot
3	Room-Room LOS	1 Static Spot
4	Corridor-Corridor LOS	2 Static Spots
5	Corridor-Corridor NLOS	2 Static Spots

Measurement data consist of so called raw data files including received IQ (In-phase and Quadrature) data. These data are further converted into Matlab compatible impulse response files and channel parameter estimates obtained using ISIS. ISIS is the processing tool of Elektrobit Testing Corporation. Parameters used in modeling (angles of arrival and departure and time delay) are estimated from these raw data using Space Alternating Generalized Expectation (SAGE) Algorithm which is already included in ISIS.

2.3 Sounder Setup

Two sets of transmitter and receiver modules are used. 50 Omni directional antenna elements (25 dual-polarized antennas) and 32 omni directional antenna elements (16 dual-polarized antennas) are used at the transmitter and the receiver, respectively. The frequency of operation is 5.25 GHz.

2.3.1 Transmitter Antenna

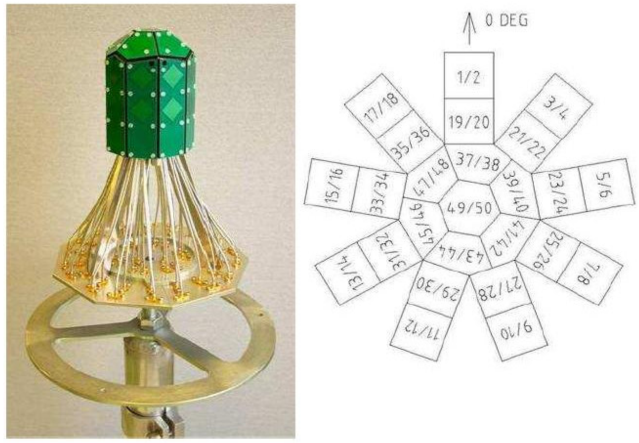

Figure 2.1: Antenna used as transmitter

Table 2.2: Transmitter antenna settings

Frequency/Bandwidth	5.25 GHz/ 8 %(420MHz)
Radiation	$\mp$ 180° Azimuth /-70°+90° Elevation
Antenna Type	Dual polarized ($\mp$ 45°) patch array, 50 elements (2x25)
Arrangement of Elements	2 rings of 9 elements, slanted ring of 6 elements plus 1 element on top

2.3.2 Receiver Antenna

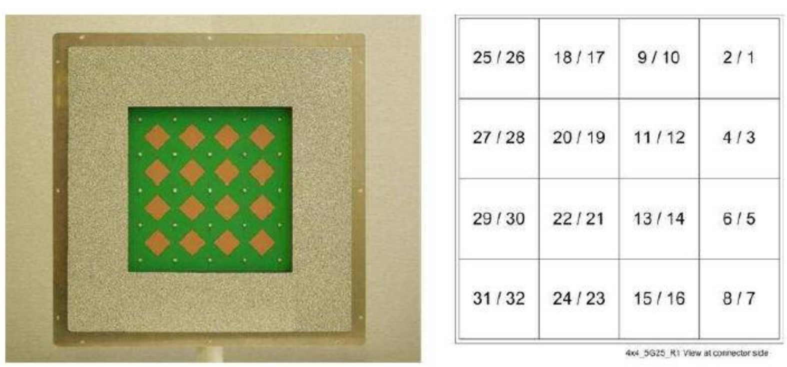

Figure 2.2: Antenna used as receiver

Table 2.3: Receiver antenna settings

Frequency/Bandwidth	5.25 GHz/ 8 %(420MHz)
Radiation	$\mp$ 70° Azimuth ; $\mp$ 70° Elevation
Antenna Type	Dual polarized ($\mp$ 45°) patch array, 32 elements (2x16)
Arrangement of Elements	4x4 square

2.3.3 Sounder Settings

Table 2.4: Channel sounder settings

Center Frequency	5.25 GHz	
Transmit Power	+26 dBm	ALC/AGC enabled, front end attenuator 0 dB
Bandwidth	200 MHz	null-to-null
Sampling Frequency	200 MHz	I and Q
Number of TX Antenna Elements	50	
Number of RX Antenna Elements	32	
Number of Channels	1600	MIMO channels (50x32)
Channel Sample Rate(trigger rate)	4 Hz	
Maximum Doppler Shift	NA	

2.4 Measurement and Scenario Parameters

During the measurements, scenario parameters listed in Table 2.5 are used. 12 different scenarios are constituted and number of cycles used in each scenario is shown in Table 2.6. Each cycle is 5 nsec period in which a single measurement is taken. Transmitter and receiver locations are shown in Figures 2.3, 2.4, 2.5, 2.6, 2.7 and 2.8, for each scenario.

Table 2.5: Scenario settings

Frequency Band	5.25 GHz / 200MHz
RX Locations	see scenario figures
RX Antenna Height	2.1-2.5m (c.a. 20cm below ceiling) To be determined within 1 cm accuracy
TX Location	see scenario figures
TX Antenna Height	1 m
Max. Path Distance	100 m (approx.)
Mobile Speed	0 m/s
Scatterer Speed	0.1 m/s
Number of Measurements	12

Table 2.6: Measurement file

#	*ScenarioDesignation*	*TXLocation*	*RXLocation*	*#ofCycles*
1.	Room-to-corridor NLOS	BS1	s68	444
2.	Corridor-to-corridor LOS	BS1	s72	436
3.	Corridor-to-corridor NLOS	BS1	s73	476
4.	Room-to-corridor NLOS	BS2	s79	444
5.	Room-to-corridor NLOS	BS2	s81	335
6.	Room-to-corridor NLOS	BS2	s82	444
7.	Room-to-room NLOS	BS3	s87	452
8.	Room-to-corridor NLOS	BS3	s88	452
9.	Room-to-corridor NLOS	BS3	s90	448
10.	Corridor-to-corridor NLOS	BS4	s124	223
11.	Corridor-to-corridor LOS	BS4	s125	236
12.	Room-to-room LOS	BS5	s143	204

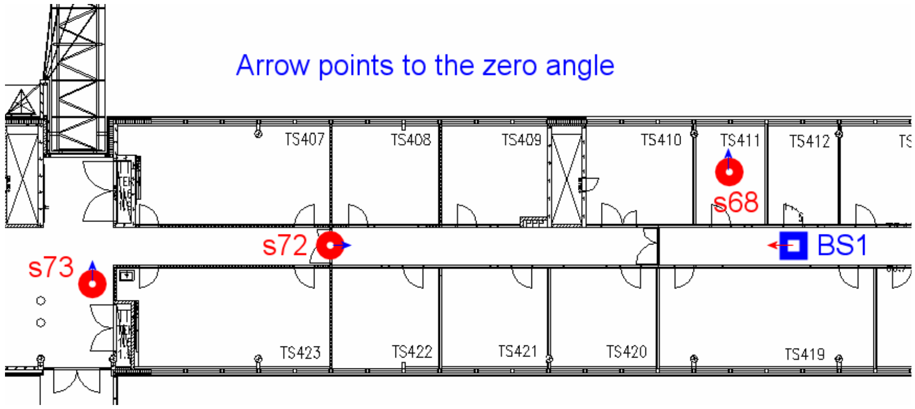

Figure 2.3: Scenario 68, 72 and 73

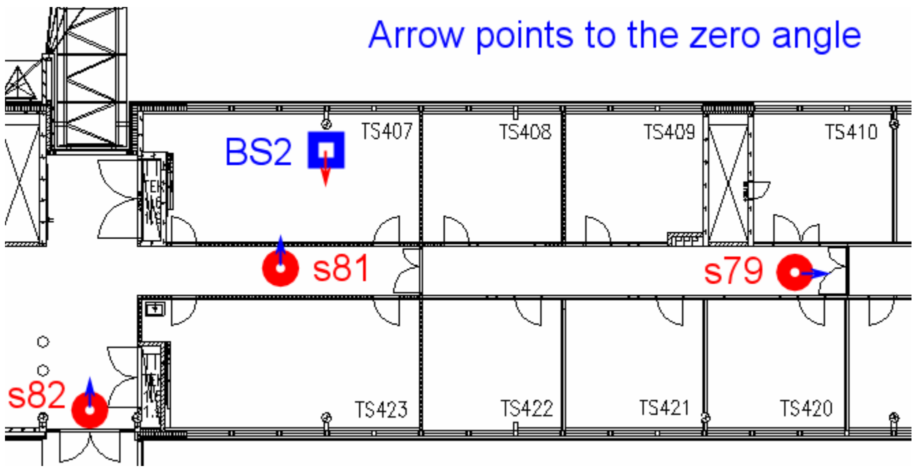

Figure 2.4: Scenario 79, 81 and 82

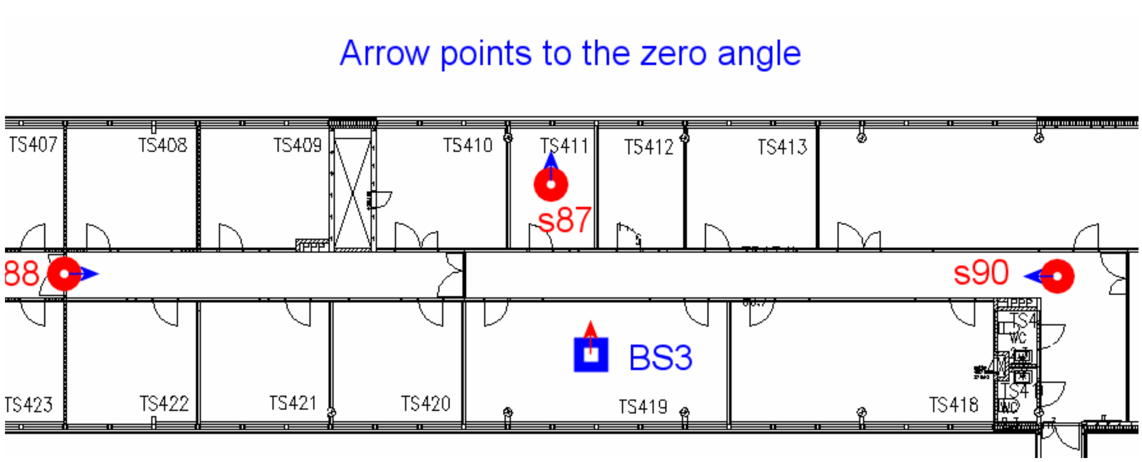

Figure 2.5: Scenario 87, 89 and 90

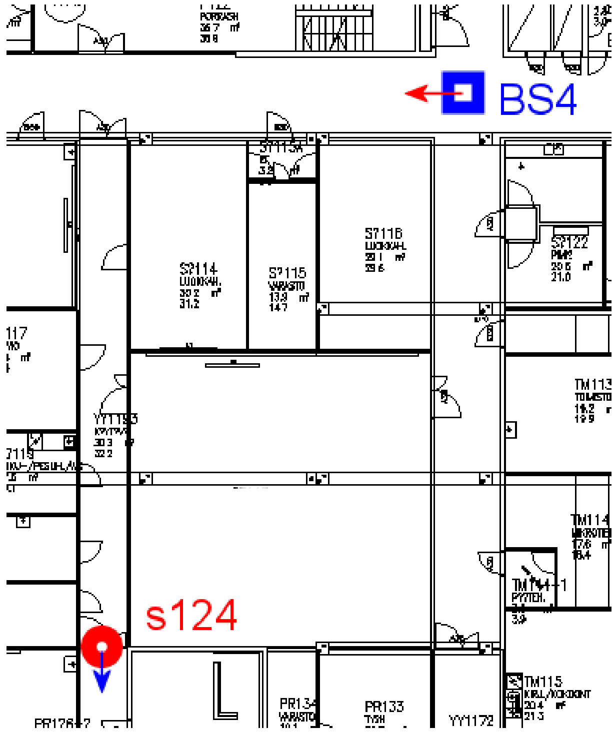

Figure 2.6: Scenario 124

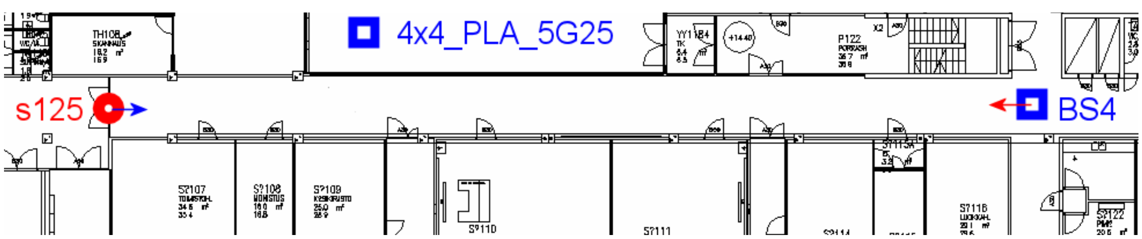

Figure 2.7: Scenario 125

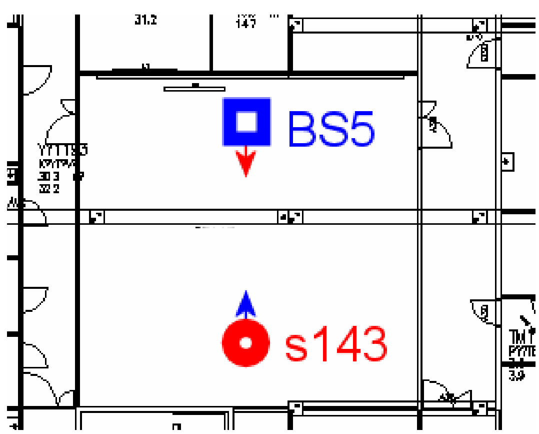

Figure 2.8: Scenario 143

2.5 SAGE Algorithm

As mentioned before, SAGE Algorithm is used to process raw data. The algorithm is used to find specular paths with multiple parameters. Delay, azimuth and elevation angles, polarizations and the complex amplitude of a known received signal are estimated [13]. These estimated parameters are used to model the channel. The algorithm is based on two steps: expectation (E-step) and maximization (M-step) steps. The E and M steps are repeated until convergence is achieved. For details of the algorithm, the reader is refered to [13].

Chapter 3

Polarized Geometric Channel Model

3.1 Introduction

Since the MIMO channel is one of the determining part of the communication system, efficient models are strongly required. Models are used to reflect the general properties of the MIMO channel for many different scenarios. There are different types of models in the literature.

In geometry-based stochastic models, the geometrical localization of scatterers are determined and the rest of the parameters of the propagation paths are defined in a stochastic way. Non-geometric stochastic models describe and determine physical parameters (angles of arrival and departure, delay, etc.) by using probability distribution functions. In deterministic physical models, the channel is modeled by ray tracing or ray launching which has to be site-specific. Another way to generate the channel model is measurement-based deterministic MIMO channel modeling. In this approach, the location of scatterers are identified from measurements [1].

Most of the channel models do not include polarization properties and the geometrical representation. To include polarization, each path has to be described in terms of two orthogonal polarizations. Because vertically polarized waves are converted into vertically and horizontally polarized waves and horizontally polarized waves are converted in the same way, too. This is because of the effect of the scatterer and modeling polarization can have a significant impact on the model complexity where in some models cross polarization ratio is treated as a random variable [1].

Proposed 3D geometric channel model in this work offers a solution to modeling polarization. In order to describe a realistic model, measurement campaign is used. Measurement data consist of channel parameter estimates like angles of arrival and departure and time delay. Using these parameters, scatterer coordinates are estimated under the single bounce assumption. Electrical properties, shapes and orientations of scatterers are obtained using Physical Optics. So each scenario can be represented with a finite number of scatterers for which locations, shapes, electrical properties and orientations are known.

3.2 Estimation of Geometric Coordinates of Scatterers

Post-processed measurement data consist of a particular number of MPCs. Each MPC is a combination of several reflections and diffractions. Locations and the number of reflections and diffractions are not known. But, angles of arrival and departure and time delay are estimated actually. So, using these estimated parameters, each MPC is modeled as a single bounce from a scatterer. Single bounce model is illustrated in Figure 3.1. The relevant parameters of the single bounce model are listed below:

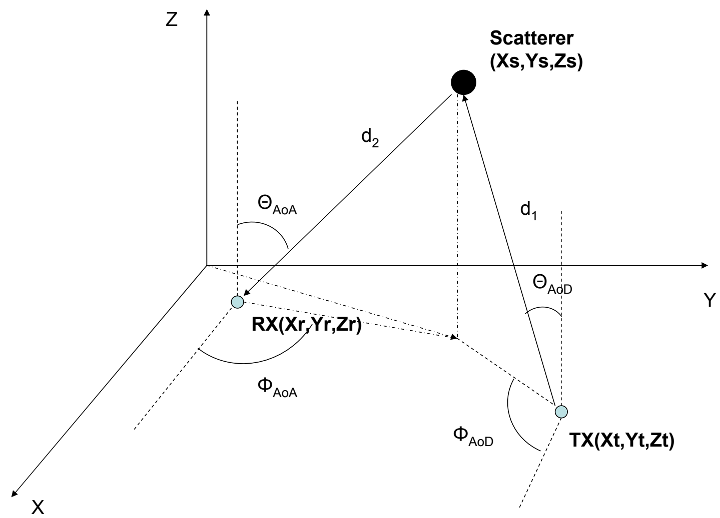

Figure 3.1: Receiver-scatterer-transmitter scenario

X_r : x coordinate of Receiver Antenna

Y_r : y coordinate of Receiver Antenna

Z_r : z coordinate of Receiver Antenna

X_t : x coordinate of Transmitter Antenna

Y_t : y coordinate of Transmitter Antenna

Z_t : z coordinate of Receiver Antenna

X_s : x coordinate of Scatterer

Y_s : y coordinate of Scatterer

Z_s : z coordinate of Scatterer

θ_{AoA} : Angle of Arrival in Elevation Plane

ϕ_{AoA} : Angle of Arrival in Azimuth Plane

θ_{AoD} : Angle of Departure in Elevation Plane

ϕ_{AoD} : Angle of Departure in Azimuth Plane

d_1 : Distance between Transmitter Antenna and Scatterer

d_1 : Distance between Receiver Antenna and Scatterer

In the single bounce model, incident wave coming from the transmitter antenna reaches the scatterer; then it scatters from the scatterer and propagates to the receiver. The geometry is shown in Figure 3.1. If a MPC in the measurement data is assumed to be a single bounce wave, then the parameters θ_{AoA}, θ_{AoD}, ϕ_{AoA}, ϕ_{AoD} and the time delay obtained from the post-processing of the measurement data fit well to the single bounce channel model and therefore it is modeled accurately.

In the multi-bounce model, incident wave coming from the transmitter antenna reaches the scatterer; then it scatters and reaches to the other scatterer(s) and propagates to the receiver. The double and the triple bounce cases are shown in Figures 3.2 and 3.3, respectively. If a MPC in the measurement data has multi scattered components, some of the parameters like θ_{AoA}, θ_{AoD}, ϕ_{AoA}, ϕ_{AoD} and the time delay will be incorrect when a single bounce model is used to represent the situation. As seen from Figure 3.4, double bounce is estimated using single bounce model shown with dashed line. If the position of the single scatterer is found such that time delay of the path is the same, other channel parameters like angles of arrival and departure will be estimated incorrectly. Hence, the measurement data will not fit to the model exactly. As the number of bounces increases, it gets difficult to model it with a single bounce model. Tolerating some error, some of the multi bounces can be modeled with single bounce model.

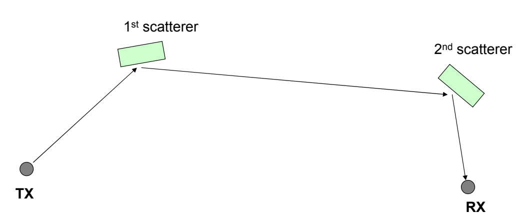

Figure 3.2: Geometry of double bounce (multi bounce) model

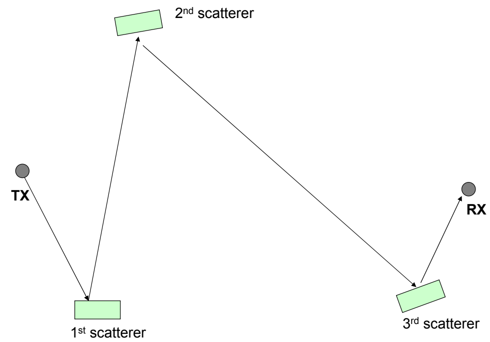

Figure 3.3: Geometry of triple bounce (multi bounce) model

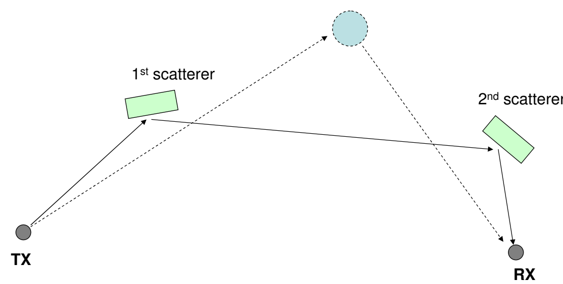

Figure 3.4: Geometry of double bounce, modeled with single bounce

A MPC beyond the error criterion is deemed as a path that can not be modeled with single bounce case, it should be modeled with multi bounce model. Since multi bounce models are complicated, single bounce model is used in this study for the MPCs within the desired error range. For this purpose, some of the parameters are assumed to have priority when compared to the remaining ones. The details of the computation are given below. Referring to Figure 3.1, the channel parameters are expressed in terms of the Cartesian coordinates of the transmitter, receiver and the scatterer. Related equations are given below:

$$\theta_{AoA} = \arctan[\frac{\sqrt{(X_s - X_r)^2 + (Y_s - Y_r)^2}}{(Z_s - Z_r)}], \tag{3.1}$$

$$\theta_{AoD} = \arctan[\frac{\sqrt{(X_s - X_t)^2 + (Y_s - Y_t)^2}}{(Z_s - Z_t)}], \tag{3.2}$$

$$\phi_{AoA} = \arctan[\frac{(Y_s - Y_r)}{(X_s - X_r)}], \tag{3.3}$$

$$\phi_{AoD} = \arctan[\frac{(Y_s - Y_t)}{(X_s - X_t)}]. \tag{3.4}$$

Total distance traveled is the sum of d_1 and d_2 in Figure 3.1. The time delay corresponding to the total distance is calculated using

$$\begin{aligned} c \cdot \tau = & \sqrt{(X_s - X_r)^2 + (Y_s - Y_r)^2 + (Z_s - Z_r)^2} \\ & + \sqrt{(X_s - X_t)^2 + (Y_s - Y_t)^2 + (Z_s - Z_t)^2} \end{aligned} \tag{3.5}$$

where τ is the time delay from the transmitter to the receiver and c is the speed of light.

Since measurement data may not be a single bounce, we need all of these equations to define the situation. Otherwise, we can define the case using four equations. These five equations define all the parameters of the problem. However, it appears that there is no unique solution for a single bounce model since there are five equations (Equations 3.1, 3.2, 3.3, 3.4 and 3.5) and three unknowns (X_s, Y_s, Z_s) and the equations are not linear. The choice of which equation is solved first becomes very important. For this purpose, percentage difference error is used as a criterion and for each parameter it is calculated according to

$$error\% = \frac{Data_{calculated} - Data_{measured}}{Data_{measured}} x100. \tag{3.6}$$

By looking at percentage difference errors of the parameters, we decided on the sequence of formulas to be used. Combinations of five equations and parameters, their solutions and results are given in the next section. The time delay is the most important parameter in terms of channel modeling since reasonable locations for scatterers are estimated. The decisive criterion on the number of multipaths to be included in the model is the value of percentage delay error.

3.3 Different Solutions to Coordinate Equations

Table 3.1: Combination of different kinds of solutions

Solution Type	Solution and Parameter Order		
Solution1-1	Equation 3.5	Equation 3.3 Equation 3.4	Equation 3.1 Equation 3.2
	X_s	Y_s	Z_s
Solution1-2	Equation 3.5	Equation 3.3 Equation 3.4	Equation 3.5
	X_s	Y_s	Z_s
Solution2-1	Equation 3.5	Equation 3.1 Equation 3.2	Equation 3.5
	X_s	Z_s	Y_s
Solution2-2	Equation 3.5	Equation 3.1 Equation 3.2	Equation 3.3 Equation 3.4
	X_s	Z_s	Y_s
Solution2-3	Equation 3.5	Equation 3.1 Equation 3.2	Equation 3.1 Equation 3.2
	X_s	Z_s	Y_s
Solution3-1	Equation 3.5	Equation 3.3 Equation 3.4	Equation 3.5
	Y_s	X_s	Z_s
Solution3-2	Equation 3.5	Equation 3.3 Equation 3.4	Equation 3.1 Equation 3.2
	Y_s	X_s	Z_s
Solution4-1	Equation 3.5	Equation 3.1 Equation 3.2	Equation 3.5
	Y_s	Z_s	X_s
Solution4-2	Equation 3.5	Equation 3.1 Equation 3.2	Equation 3.3 Equation 3.4
	Y_s	Z_s	X_s
Solution4-3	Equation 3.5	Equation 3.1 Equation 3.2	Equation 3.1 Equation 3.2
	Y_s	Z_s	X_s

Solution Type	Solution and Parameter Order		
Solution5-1	Equation 3.5	Equation 3.5	Equation 3.3 Equation 3.4
	Z_s	X_s	Y_s
Solution5-2	Equation 3.5	Equation 3.5	Equation 3.1 Equation 3.2
	Z_s	X_s	Y_s
Solution6-1	Equation 3.5	Equation 3.5	Equation 3.3 Equation 3.4
	Z_s	Y_s	X_s
Solution6-2	Equation 3.5	Equation 3.5	Equation 3.1 Equation 3.2
	Z_s	Y_s	X_s
Solution6-3	Equation 3.5	Equation 3.5	Equation 3.5
	Z_s	Y_s	X_s

15 different solutions are shown in Table 3.3. The parameter and the equation in the second column is solved first. In the next step, the parameter and the equation in the third column is solved and finally fourth column is solved. Solution order of equations and the sequence of parameters are very important. Some of the solution types do not yield real valued solutions and some give unreasonably big parameters. All solution types are processed over 444 cycles for scenario 68 and 436 cycles for scenario 72.

Each cycle includes approximately 50 MPCs and each ISIS processed MPC has parameters like θ_{AoA}, θ_{AoD}, ϕ_{AoA}, ϕ_{AoD} and τ. Using the parameters, estimated locations of scatterers (X_s, Y_s, Z_s) are calculated using Equations 3.1, 3.2, 3.3, 3.4 and 3.5. Finally, using Equation 3.5 and calculated scatterer locations, estimated time delay is found. Difference of the actual and the estimated delay is used to determine percentage delay error. This procedure is applied to every MPC in each cycle. Number of multipaths within 10 percentage delay error are considered as distinctive criterion. For the moment 10 percentage delay error is chosen, but a detailed study for deciding on the percentage delay error will be explained in the next section. The schematic illustration of the flow of the procedure is shown below:

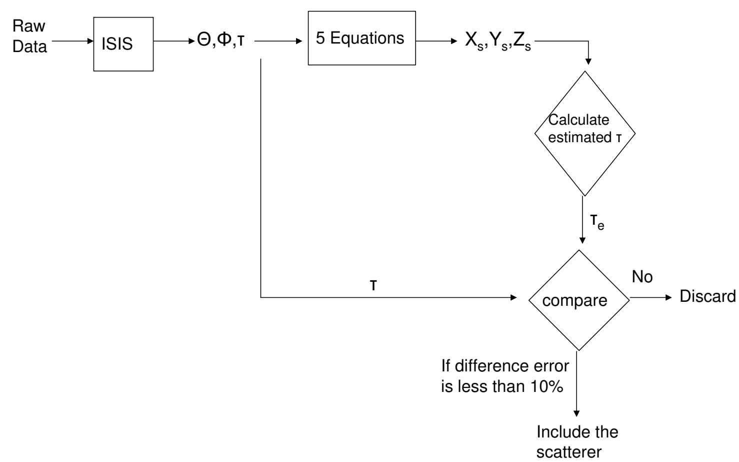

Figure 3.5: Schematic illustration of the procedure

For each cycle, the number of multipaths within the desired range is calculated and averaged over 444 cycles for scenario 68 and 436 cycles for scenario 72, seperately. Aim is to find the most appropriate procedure for single bounce modeling and criterion is the highest average number of multipaths. MATLAB is used as processing tool. Results are presented in detail below.

3.3.1 Solution 1-1

In this solution type X_s, Y_s, Z_s are found respectively by using Equation 3.5, Equations 3.3-3.4 and Equations 3.1-3.2, respectively.

Using Equation 3.3 and then Equations 3.1 and 3.7, we get

$$(Y_s - Y_r) = \tan\phi_{AoA}(X_s - X_r) \tag{3.7}$$

and

$$(Z_s - Z_r) = \frac{|X_s - X_r|\sqrt{1 + \tan^2\phi_{AoA}}}{\tan\theta_{AoA}} \tag{3.8}$$

Similarly, using Equation 3.4 and then Equations 3.2 and 3.9, we get

$$(Y_s - Y_t) = \tan\phi_{AoD}(X_s - X_t) \tag{3.9}$$

and

$$(Z_s - Z_t) = \frac{|X_s - X_t|\sqrt{1 + \tan^2\phi_{AoD}}}{\tan\theta_{AoD}} \tag{3.10}$$

If we insert Equations 3.7, 3.8, 3.9 and 3.10 into Equation 3.5, we obtain

$$\begin{aligned} c\tau = |X_s - X_r|\sqrt{1 + \tan^2\phi_{AoA} + \frac{1 + \tan^2\phi_{AoA}}{\tan^2\theta_{AoA}}} + \\ +|X_s - X_t|\sqrt{1 + \tan^2\phi_{AoD} + \frac{1 + \tan^2\phi_{AoD}}{\tan^2\theta_{AoD}}} \end{aligned} \tag{3.11}$$

Only unknown X_s is found from this equation. Then, Y_s is found from Equations 3.7 and 3.9 as follows:

$$Y_s = Y_r + \tan\phi_{AoA}(X_s - X_r) \tag{3.12}$$

$$Y_s = Y_t + \tan\phi_{AoD}(X_s - X_t) \tag{3.13}$$

Finally, Z_s is found as

$$Z_s = Z_r + \frac{\sqrt{(X_s - X_r)^2 + (Y_s - Y_r)^2}}{\tan\theta_{AoA}} \tag{3.14}$$

$$Z_s = Z_t + \frac{\sqrt{(X_s - X_t)^2 + (Y_s - Y_t)^2}}{\tan\theta_{AoD}} \tag{3.15}$$

Note that two different values of Y_s are obtained from Equations 3.12 and 3.13. Similarly, two different values of Z_s are obtained from Equations 3.14 and 3.15. Therefore, there are 4 different solution sets. This procedure gives real X_s, Y_s and Z_s values. But the number of multipaths within the desired range is not high enough. Hence, this procedure is considered as inappropriate for our model.

3.3.2 Solution 1-2

In this solution type X_s, Y_s, Z_s are found respectively by using Equation 3.5, Equations 3.3-3.4 and Equation 3.5 respectively. X_s and Y_s are found in the same manner explained in Subsection 3.3.1. Using the values of X_s and Y_s, Z_s is found from Equation 3.5.

Note that two different values of Y_s are obtained from Equations 3.12 and 3.13. Two different values of Z_s are obtained from the second order solution of Equation 3.5. Therefore, there are 4 different solution sets. This procedure gives reasonable X_s and Y_s values but could not find a Z_s solution to every X_s-Y_s pair. So, this method is considered as inappropriate for our model.

3.3.3 Solution 2-1

In this solution type X_s, Z_s, Y_s are found respectively by using Equation 3.5, Equations 3.1-3.2 and Equation 3.5 respectively. X_s is found in the same manner explained in Subsection 3.3.1. Z_s is found as follows

$$Z_s = Z_r + \frac{|X_s - X_r|\sqrt{1 + \tan^2 \phi_{AoA}}}{\tan \theta_{AoA}} \tag{3.16}$$

$$Z_s = Z_t + \frac{|X_s - X_t|\sqrt{1 + \tan^2 \phi_{AoD}}}{\tan \theta_{AoD}} \tag{3.17}$$

Using the values of X_s and Z_s, Y_s is found from Equation 3.5.

Note that two different values of Z_s are obtained from Equations 3.16 and 3.17. Two different values of Y_s are obtained from the second order solution of Equation 3.5. Therefore, there are 4 different solution sets. This procedure gives reasonable X_s and Z_s values but could not find a Y_s solution to every X_s-Z_s pair. If only percentage delay error is 0, it finds a solution otherwise not. So this procedure is considered as inappropriate for our model.

3.3.4 Solution 2-2

In this solution type X_s, Z_s, Y_s are found respectively by using Equation 3.5, Equations 3.1-3.2 and Equations 3.3-3.4 respectively. X_s is found in the same manner explained in Subsection 3.3.1. Z_s is found using Equations 3.16 and 3.17. Finally , Y_s is found from Equations 3.12 and 3.13.

Note that two different values of Z_s are obtained from Equations 3.16 and 3.17. Similarly, two different values of Y_s are obtained from Equations 3.12 and 3.13. Therefore, there are 4 different solution sets. This procedure gives real X_s, Z_s and $Y_s$values. But the number of multipaths within the desired range is not high enough. So this procedure is considered as inappropriate for our channel model.

3.3.5 Solution 2-3

In this solution type X_s, Z_s, Y_s are found respectively by using Equation 3.5, Equations 3.1-3.2 and Equations 3.1-3.2 respectively. X_s is found in the same manner explained in Subsection 3.3.1. Z_s is found using Equations 3.16 and 3.17. Finally, using Equations 3.1 and 3.2, Y_s is found as follows:

$$Y_s = Y_r + \sqrt{(Z_s - Z_r)^2 \tan^2 \theta_{AoA} - (X_s - X_r)^2} \tag{3.18}$$

and

$$Y_s = Y_t + \sqrt{(Z_s - Z_t)^2 \tan^2 \theta_{AoD} - (X_s - X_t)^2} \tag{3.19}$$

Note that two different values of Z_s are obtained from Equations 3.16 and 3.17. Similarly, two different values of Y_s are obtained from Equations 3.18 and 3.19. Therefore, there are 4 different solution sets. This procedure gives real X_s, Z_s and Y_s values. But the number of multipaths within the desired range is not high enough. So Solution2-3 is considered as inappropriate for our model.

3.3.6 Solution 3-1

In this solution type Y_s, X_s, Z_s are found respectively by using Equation 3.5, Equations 3.3-3.4 and Equation 3.5 respectively.

Using Equation 3.3 and then Equations 3.1 and 3.20, we get

$$(X_s - X_r) = \frac{(Y_s - Y_r)}{\tan\phi_{AoA}} \tag{3.20}$$

and

$$(Z_s - Z_r) = |Y_s - Y_r| \frac{\sqrt{\frac{1}{\tan^2\phi_{AoA}} + 1}}{\tan\theta_{AoA}} \tag{3.21}$$

Similarly, using Equation 3.4 and then Equations 3.2 and 3.22, we get

$$(X_s - X_t) = \frac{(Y_s - Y_t)}{\tan\phi_{AoD}} \tag{3.22}$$

and

$$(Z_s - Z_t) = |Y_s - Y_t| \frac{\sqrt{\frac{1}{\tan^2\phi_{AoD}} + 1}}{\tan\theta_{AoD}} \tag{3.23}$$

Inserting Equations 3.20, 3.21, 3.22 and 3.23 into Equation 3.5, we obtain:

$$\begin{aligned} c\tau = {} & |Y_s - Y_r| \sqrt{\frac{1}{\tan^2\phi_{AoA}} + \frac{\frac{1}{\tan^2\phi_{AoA}} + 1}{\tan^2\theta_{AoA}} + 1} + \\ & + |Y_s - Y_t| \sqrt{\frac{1}{\tan^2\phi_{AoD}} + \frac{\frac{1}{\tan^2\phi_{AoD}} + 1}{\tan^2\theta_{AoD}} + 1} \end{aligned} \tag{3.24}$$

Only unknown Y_s is found from this equation. Then, X_s is found from Equations 3.20 and 3.22 as follows:

$$X_s = X_r + \frac{(Y_s - Y_r)}{\tan\phi_{AoA}} \tag{3.25}$$

$$X_s = X_t + \frac{(Y_s - Y_t)}{\tan\phi_{AoD}} \tag{3.26}$$

Finally, Z_s is found from Equation 3.5.

Note that two different values of X_s are obtained from Equations 3.25 and 3.26. Two different values of Z_s are obtained from second order solution of Equation 3.5. Therefore, there are 4 different solution sets. The method gives real X_s and Y_s values but could not find a Z_s solution to every X_s-Y_s pair. So this procedure is considered as inappropriate for our model.

3.3.7 Solution 3-2

In this solution type Y_s, X_s, Z_s are found respectively by using Equation 3.5, Equations 3.3-3.4 and Equations 3.1-3.2 respectively. Y_s and X_s are found in the same manner explained in Subsection 3.3.6. Z_s is found using Equations 3.14 and 3.15.

Note that two different values of X_s are obtained from Equations 3.25 and 3.26. Similarly, two different values of Z_s are obtained from Equations 3.14 and 3.15. Therefore, there are 4 different solution sets. The method gives real Y_s, X_s and Z_s values. But the number of multipaths within the desired range is not high enough. So this procedure is considered as inappropriate for our model.

3.3.8 Solution 4-1

In this solution type Y_s, Z_s, X_s are found respectively by using Equation 3.5, Equations 3.1-3.2 and Equation 3.5 respectively. Y_s is found in the same manner explained in Subsection 3.3.6. Z_s is found using Equations 3.21 and 3.23. Finally, X_s is found from Equation 3.5.

Note that two different values of Z_s are obtained from Equations 3.21 and 3.23. Two different values of X_s are obtained from second order solution of Equation 3.5. Therefore, there are 4 different solution sets. The method gives real Y_s and Z_s values but could not find an X_s solution to every Y_s-Z_s pair. If only percentage delay error is 0, it finds a solution otherwise not. So this procedure is considered as inappropriate for our model.

3.3.9 Solution 4-2

In this solution type Y_s, Z_s, X_s are found respectively by using Equation 3.5, Equations 3.1-3.2 and Equations 3.3-3.4 respectively. Y_s is found in the same manner explained in Subsection 3.3.6. Z_s is found using Equation 3.21 and Equation 3.23. Finally, X_s is found from Equations 3.20 and 3.22.

Note that two different values of Z_s are obtained from Equations 3.21 and 3.23. Similarly, two different values of X_s are obtained from Equations 3.20 and 3.22. Therefore, there are 4 different solution sets. The method gives real Y_s, X_s and Z_s values. But the number of multipaths within the desired range is not high enough. So this procedure is considered as inappropriate for our model.

3.3.10 Solution 4-3

In this solution type Y_s, Z_s, X_s are found respectively by using Equation 3.5, Equations 3.1-3.2 and Equations 3.1-3.2 respectively. Y_s is found in the same manner explained in Subsection 3.3.6. Z_s is found using Equation 3.21 and Equation 3.23. Finally, X_s is found as follows:

$$X_s = X_r + \sqrt{(Z_s - Z_r)^2 \tan^2 \theta_{AoA} - (Y_s - Y_r)^2} \tag{3.27}$$

and

$$X_s = X_t + \sqrt{(Z_s - Z_t)^2 \tan^2 \theta_{AoD} - (Y_s - Y_t)^2} \tag{3.28}$$

Note that two different values of Z_s are obtained from Equations 3.21 and 3.23. Similarly, two different values of X_s are obtained from Equations 3.27 and 3.28. Therefore, there are 4 different solution sets. The method gives real Y_s, X_s and Z_s values. But the number of multipaths within the desired range is not high enough. So this procedure is considered as inappropriate for our model.

3.3.11 Solution 5-1

In this solution type Z_s, X_s, Y_s are found respectively by using Equation 3.5, Equation 3.5 and Equations 3.3-3.4 respectively.

Taking squares of both sides of Equations 3.1 and 3.2, we get

$$(X_s - X_r)^2 + (Y_s - Y_r)^2 = (Z_s - Z_t)^2 \tan^2 \theta_{AoA} \tag{3.29}$$

and

$$(X_s - X_t)^2 + (Y_s - Y_t)^2 = (Z_s - Z_r)^2 \tan^2 \theta_{AoD} \tag{3.30}$$

Using these two equalities in Equation 3.5, we obtain

$$c\tau = |Z_s - Z_r|\sqrt{1 + \tan^2 \theta_{AoA}} + |Z_s - Z_t|\sqrt{1 + \tan^2 \theta_{AoD}} \tag{3.31}$$

Z_s is found from this equation. And X_s is found from Equation 3.11. Using the value of X_s, Y_s is found from Equations 3.12 and 3.13.

Note that two different values of Y_s are obtained from Equations 3.12 and 3.13. Therefore, there are 2 different solution sets. The method gives real Z_s, X_s and Y_s values. For the 2^{nd} solution set, the number of multipaths within the desired range is the highest value obtained among all solution types.

Second Z_s,X_s,Y_s solution set : An average number of 9.7798 multipaths for scenario 72 and 18.5991 multipaths for scenario 68 are obtained. Related figures are given below.

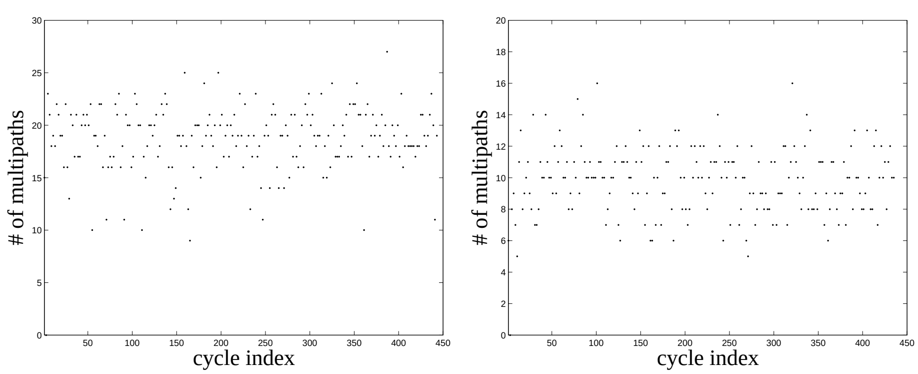

Figure 3.6: Solution5-1, 2^{nd} solution, scenario 68 and scenario 72 respectively

3.3.12 Solution 5-2

In this solution type Z_s, X_s, Y_s are found respectively by using Equation 3.5, Equation 3.5 and Equations 3.1-3.2 respectively.

Z_s and X_s are found in the same manner explained in Subsection 3.3.11. Using the values of Z_s and X_s, Y_s is found from Equation 3.18 and Equation 3.19.

Note that two different values of Y_s are obtained from Equations 3.18 and 3.19. Therefore, there are 2 different solution sets. The method gives real X_s and Z_s values but could not find a Y_s solution to every X_s-Z_s pair. If only percentage delay error is very small, it finds a solution; otherwise not. So this procedure is considered as inappropriate for our model.

3.3.13 Solution 6-1

In this solution type Z_s, Y_s, X_s are found respectively by using Equation 3.5, Equation 3.5 and Equations 3.3-3.4 respectively. Z_s is found in the same manner explained in Subsection 3.3.11. Y_s is found using Equation 3.24. Finally, X_s is found from Equations 3.20 and 3.22.

Note that two different values of X_s are obtained from Equations 3.20 and 3.22. Therefore, there are 2 different solution sets. The method gives real Z_s, Y_s and X_s values. The average number of multipaths (average of the number of multipaths obtained for two scenarios) within the desired range is high but is a bit lower for scenario 72 than the number obtained in 2^{nd} solution set of Solution5-1.

3.3.14 Solution 6-2

In this solution type Z_s, Y_s, X_s are found respectively by using Equation 3.5, Equation 3.5 and Equations 3.1-3.2 respectively. Z_s is found in the same manner explained in Subsection 3.3.11. Y_s is found using Equation 3.24. Finally, X_s is found from Equations 3.27 and 3.28.

Note that two different values of X_s are obtained from Equations 3.27 and 3.28. Therefore, there are 2 different solution sets. The method gives real Y_s and Z_s values but could not find an X_s solution to every Y_s-Z_s pair. If only percentage delay error is 0, it finds a solution; otherwise not. So this procedure is considered as inappropriate for our model.

3.3.15 Solution 6-3

In this solution type Z_s, Y_s and X_s are all found by using Equation 3.5. Z_s is found in the same manner explained in Subsection 3.3.11. Y_s and X_s are found using Equations 3.24 and 3.11, respectively.

There is 1 solution set. The method gives real Y_s and Z_s values but could not find an X_s solution to every Y_s-Z_s pair. So this procedure is considered as inappropriate for our model.

The results are summarized in Table 3.2.

Table 3.2: Average number of multipaths for each scenario and solution type

	1. Solution Set		2. Solution Set		3. Solution Set		4. Solution Set	
	Scenario							
	72	68	72	68	72	68	72	68
Solution1-1	2.1422	0.1982	1.3532	0.2252	2.6697	2.9459	3.422	0.2748
Solution1-2	-	-	-	-	-	-	-	-
Solution2-1	-	-	-	-	-	-	-	-
Solution2-2	2.1284	0.1982	3.1972	9.7838	2.0092	0.4054	3.422	0.2748
Solution2-3	2.1284	0.1847	2.1147	0.3559	2.9312	1.3559	3.3899	2.2117
Solution3-1	-	-	-	-	-	-	-	-
Solution3-2	1.945	2.4865	1.5046	1.7072	2.8991	0.3243	0.2523	0.4009
Solution4-1	-	-	-	-	-	-	-	-
Solution4-2	1.945	2.4865	0.5734	0.3198	1.8349	7.0315	0.2523	0.4009
Solution4-3	1.8761	1.9865	1.945	2.3514	0.2523	0.3694	0.1284	0.2432
Solution5-1	7.8899	2.6667	9.7798	18.5991	-	-	-	-
Solution5-2	-	-	-	-	-	-	-	-
Solution6-1	7.1789	18.7027	8.2431	5.473	-	-	-	-
Solution6-2	-	-	-	-	-	-	-	-
Solution6-3	-	-	-	-	-	-	-	-

For each solution type, the average number of multipaths is shown for each solution set considering two scenarios. As mentioned before, for some solution types, real values of parameters could not be obtained. Solutions 5-1 and 6-1 have only two solution sets. Also, second solution set of Solution5-1 has the highest average (average of two scenarios) number of multipaths within the desired range. Estimated locations of scatterers are also found at reasonable coordinates when bounds of scenarios are considered. So second solution set of Solution5-1 is considered as the most appropriate method for our channel model.

3.4 Synthetic Scenarios

In order to see if coordinates of scatterers are estimated at reasonable locations and since locations of scatterers in measurement data are not known, synthetic data corresponding to measurement scenarios are created. For this purpose, percentage delay error is used. The number and locations of scatterers are chosen randomly. Single, double and triple bounces are included in synthetic scenarios. Double and triple bounces are used to scale percentage delay error in modeling the MPC as a single bounce model. Bouncing from two scatterers is modeled as if it is scattered by a single scatterer and an estimated location is found for the scatterer. If the estimated location is close to the locations of these two scatterers, this double bounce is assumed to be represented by single bounce model; if not, it can not be represented. This procedure is summarized in :

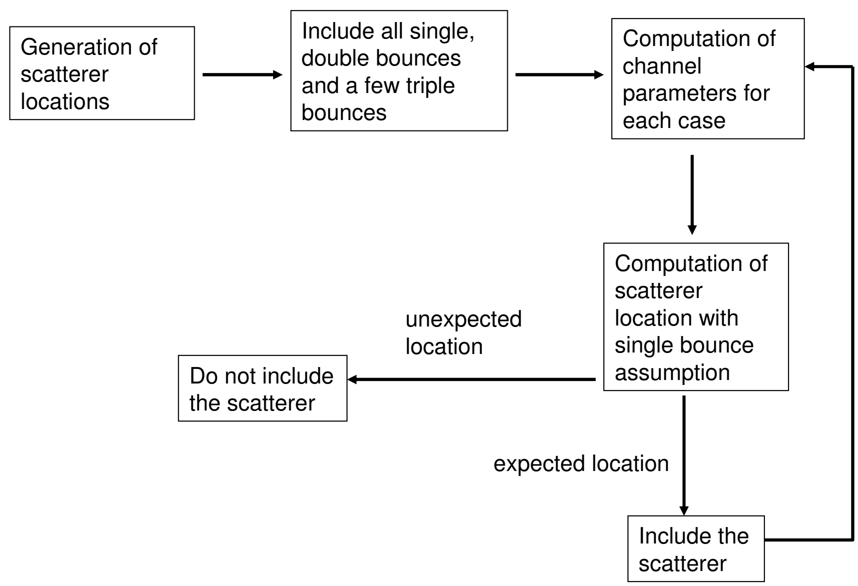

Figure 3.7: Schematic illustration of synthetic data computation

This work is applied to two scenarios (scenario68 and scenario72) using MATLAB.

Scenario 68 :

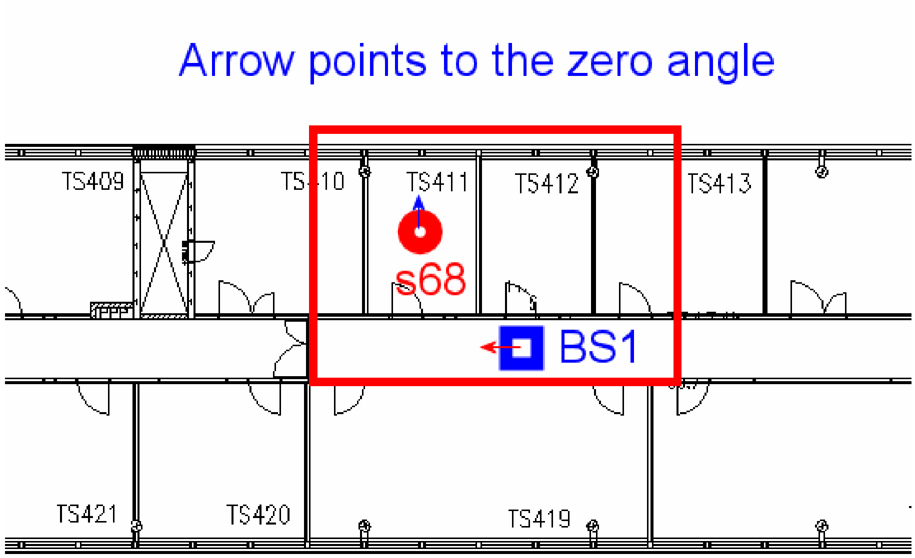

Figure 3.8: Measurement environment, scenario 68

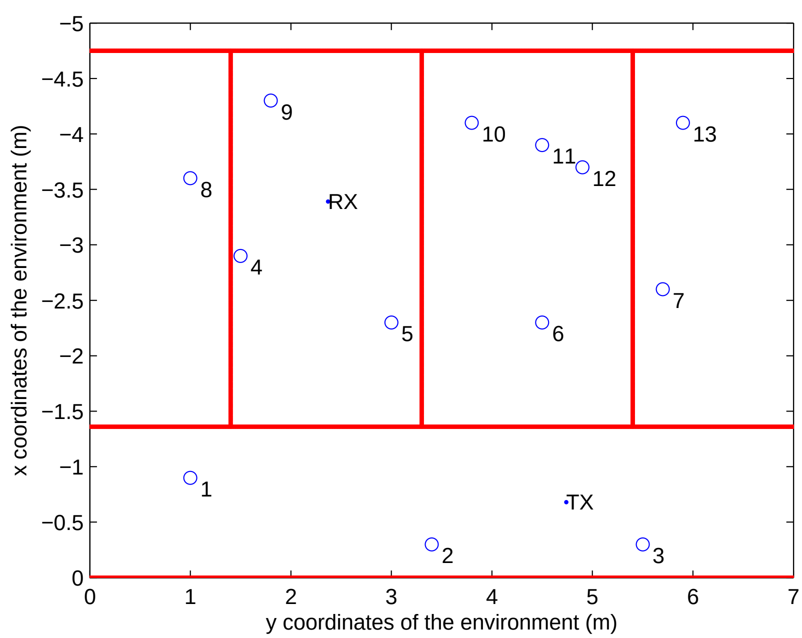

Figure 3.9: Scenario 68 adapted from the measurement environment

Real measurement environment and the adapted scenario are shown in Figures 3.8 and 3.9, respectively. Each symbol "o" represents a scatterer and

13 scatterers are distributed around. Solution is obtained by using Solution5-1. Table 3.3 shows the results of single bounce modeling.

Table 3.3: Single bounce model, synthetic scenario 68

scatterer	X_s (m)	Y_s (m)	Z_s (m)	*delay* (ns)	difference error *delay*(%)	θ_{AoA}	θ_{AoD}	ϕ_{AoA}	ϕ_{AoD}
1	-0.9	1	1.5	22.44	0	0	0	0	0
2	-0.3	3.4	2	16.62	0	0	0	0	0
3	-0.3	5.5	1.8	18.65	0	0	0	0	0
4	-2.9	1.5	2.2	17.03	0	0	0	0	0
5	-2.3	3	1.8	12.88	0	0	0	0	0
6	-2.3	4.5	1.9	14.32	0	0	0	0	0
7	-2.6	5.7	1.4	19.08	0	0	0	0	0
8	-3.6	1	2.5	21.26	0	0	0	0	0
9	-4.3	1.8	0.3	23.29	0	0	0	0	0
10	-4.1	3.8	2	17.70	0	0	0	0	0
11	-3.9	4.5	2	18.64	0	0	0	0	0
12	-3.7	4.9	2	19.17	0	0	0	0	0
13	-4.1	5.9	1.2	24.61	0	0	0	0	0

Table 3.4: Double bounce model, synthetic scenario 68

scatterer 1^{st}	2^{nd}	X_s (m)	Y_s (m)	Z_s (m)	*delay* (ns)	difference error *delay*(%)	θ_{AoA}	θ_{AoD}	ϕ_{AoA}	ϕ_{AoD}
7	11	-3.97	4.8	2.74	20.88	0.11	17.73	17.26	0	25.57
11	10	-4.26	4.11	1.64	19.11	0.13	8.04	7.17	0	5.69
12	10	-4.32	4.25	1.48	19.93	0.28	10.8	10.94	0	4.61
13	10	-4.77	5.15	1.04	24.96	0.29	11.50	2.68	0	12.97
12	11	-3.94	4.68	1.89	19.48	0.78	1.91	3	0	2.03
10	9	-4.98	1.38	3.79	28.63	0.78	10.26	11.33	0	22.69
5	9	-4.22	1.85	4.04	25.17	0.93	22.36	15.01	0	7.82
11	12	-3.77	5.47	1.91	21.31	0.99	0.33	1.16	0	9.11
10	11	-4.07	5.23	1.8	22.08	1.83	1.81	2.58	0	7.19
7	13	-4.07	5.76	2.49	24.92	2.26	20.06	12.2	0	9.81
10	12	-3.87	6.3	1.76	24.74	2.72	1.06	3.67	0	10.64
6	10	-4.06	3.72	1.48	18.09	2.82	17.88	21	0	8.42
9	11	-4.56	7.27	0.96	33.81	2.92	7.1	8.04	0	6.01
13	11	-4.24	5.92	0.8	24.84	3.39	14.51	6.2	0	0.36
11	9	-5.09	1.31	4.29	29.55	5.03	16.52	13.29	0	33.65
6	12	-3.68	4.77	1.81	19.65	5.45	4.84	13.76	0	7.94
6	11	-3.86	4.32	1.74	18.94	5.57	7.94	15.85	0	0.81
8	9	-4.6	1.61	4.76	32.3	5.93	31.72	19.36	0	13.43
9	13	-4.78	9.26	0.19	42.28	6.36	0.27	0.97	0	8.73

9	12	-4.16	8.62	1.02	36.23	7.06	4.81	8.72	0	9.06
scatterer		X_s	Y_s	Z_s	*delay*	difference error				
1^{st}	2^{nd}	(m)	(m)	(m)	(ns)	*delay*(%)	θ_{AoA}	θ_{AoD}	ϕ_{AoA}	ϕ_{AoD}
13	12	-3.89	6.44	0.62	25.08	7.44	15.52	9.1	0	9.21
8	12	-4.08	7.98	0.93	38.25	8.48	6.9	18.37	0	8.41
4	8	-3.55	1.29	2.49	21.39	9.12	1.63	1.36	0	5.42
12	9	-5.13	1.28	4.69	30.14	9.41	21.07	14.9	0	34.83
1	10	-1.5	-1.44	2.23	32.29	9.63	9.75	3.59	0	4.15
5	8	-3.66	0.62	2.53	21.32	10.8	0.83	1.85	0	7.07
9	10	-4.91	5.42	0.84	29.91	10.94	12.53	6.41	0	29.9
4	9	-4.25	1.83	4.18	29.19	11.61	33.41	17.65	0	16.41
7	9	-4.98	1.38	2.71	29.49	13.71	16.03	6.79	0	11.49
13	9	-5.42	1.1	1.51	33.63	15.46	43.51	1.69	0	18.79
3	2	0.21	3.57	1.81	21.83	15.92	2.13	14.5	0	10.73
8	10	-4.61	4.83	-0.17	31.63	17.9	31.33	44.09	0	29.25
8	11	-4.4	6.6	0.71	35.78	18.01	12.22	21.46	0	25.47
3	5	-0.13	4.25	-0.76	19.08	18.03	17.48	20.69	0	21.64
1	6	-0.95	7.15	2.41	33.32	18.25	10.7	22.66	0	2.92
5	10	-3.89	3.38	1.41	20.38	19.08	27.85	11.95	0	24.03
6	7	-2.3	6.95	0.12	22.47	19.7	10.09	43.46	0	44.69
5	12	-3.72	5.07	1.68	24.81	20.47	6.17	6.08	0	40.91
4	12	-3.9	6.53	1.19	33.91	21.15	8.2	14.11	0	26.55
3	1	0.6	0.17	-0.73	28.89	21.39	17.94	26.63	0	10.89
5	11	-3.85	4.3	1.63	23.07	22.5	10.86	7.5	0	39.23

When we look at the Table 3.3, the method finds the locations of scatterers exactly since they are all single bounce cases (All % errors are zero). X_s, Y_s and Z_s are the calculated coordinates of the scatterers in the synthetic scenario 68.

Table 3.5: Triple bounce model, synthetic scenario 68

scatterer			X_s	Y_s	Z_s	*delay*	difference error				
1^{st}	2^{nd}	3^{rd}	(m)	(m)	(m)	(ns)	*delay*(%)	θ_{AoA}	θ_{AoD}	ϕ_{AoA}	ϕ_{AoD}
12	11	10	-4.32	4.25	1.47	19.95	0.28	10.82	10.97	0	4.56
7	12	11	-3.98	4.85	2.70	21.09	0.49	16.78	16.69	0	24.7

In Table 3.4, estimated locations of scatterers are given with increasing order of percentage delay error. There are 156 different cases but only a potrion of them is shown in the table. As percentage delay error increases, estimation of locations gets worse as expected. Also, triple bounces are shown in Table 3.5.

For triple bounce, only scatterers which are close to each other are chosen. Hence, reasonable locations are estimated using single bounce model with small percentage delay errors. By looking at Tables 3.4 and 3.5, estimated coordinates of scatterers are investigated and cases which have percentage delay error below seven are considered to be reasonable ones. Beyond seven percentage delay error, most of the cases can not be modeled with reasonable locations of single scatterers. For illustration purposes, some examples with different delay errors are given below.

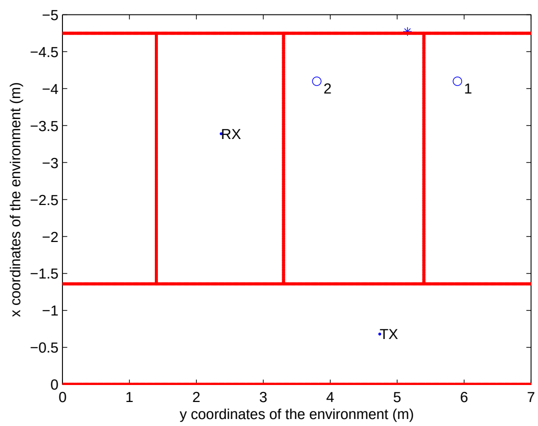

Figure 3.10: Single bounce model, scenario 68, 0.29 % delay error

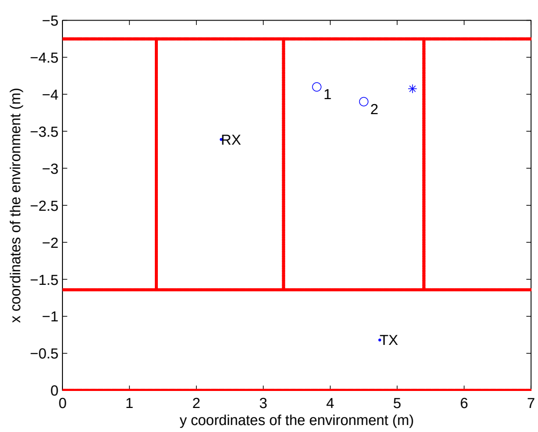

Figure 3.11: Single bounce model, scenario 68, 1.83 % delay error

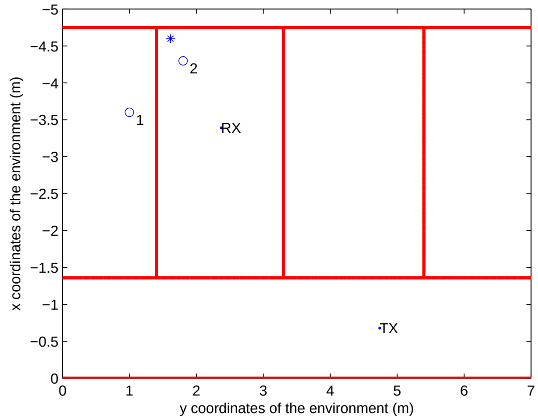

Figure 3.12: Single bounce model, scenario 68, 5.94 % delay error

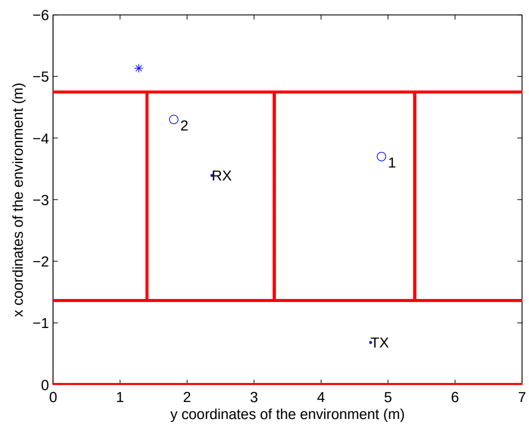

Figure 3.13: Single bounce model, scenario 68, 9.41 % delay error

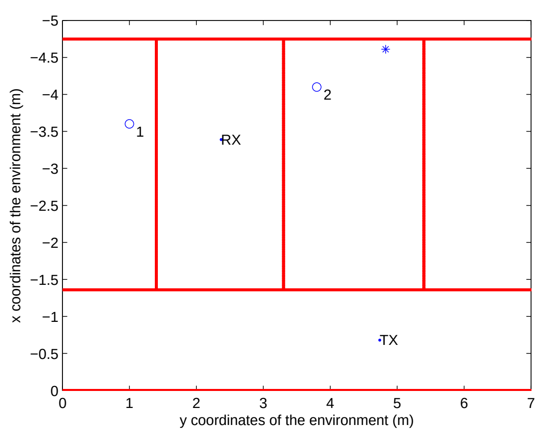

Figure 3.14: Single bounce model, scenario 68, 17.90 % delay error

where each '∘' represents a synthetically placed scatterer and each '∗' represents the estimated position for the single bounce model. Figures 3.10, 3.11 and 3.12 represent the cases which can be modeled with single bounce model. Estimated locations are close to both of the scatterers. Figures 3.13 and 3.14 represent the cases which are considered not to be modeled with single bounce model.

Scenario 72 :

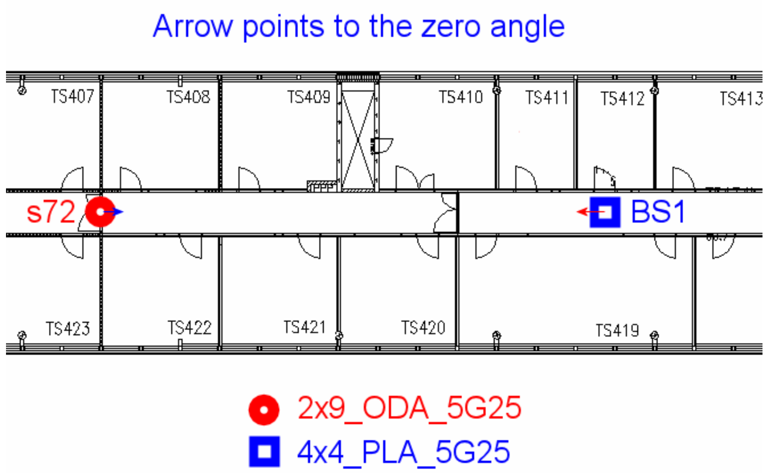

Figure 3.15: Scenario 72

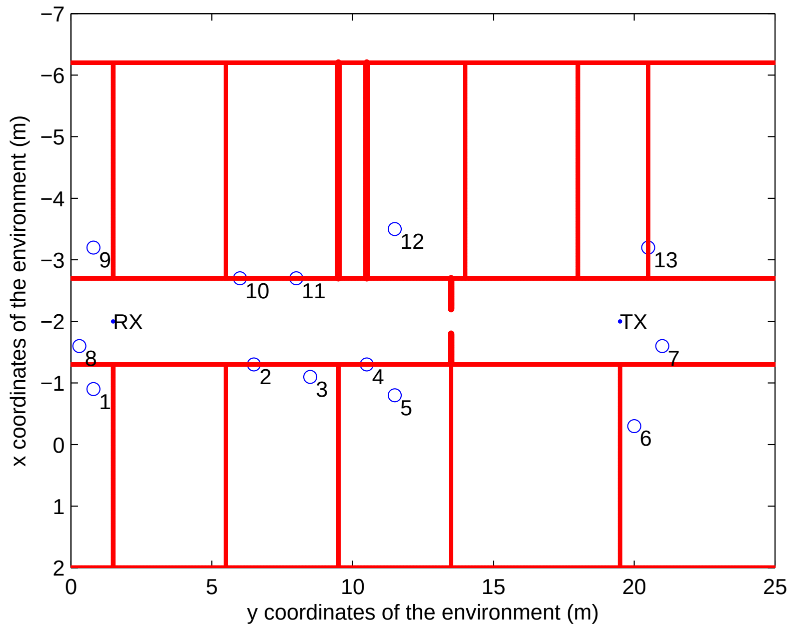

Figure 3.16: Scenario 72 adapted from the measurement environment

Real measurement environment and the adapted scenario are shown in Figures 3.15 and 3.16, respectively. Each symbol "o" represents a scatterer and 13 scatterers are distributed around. Coordinate equations are solved by using solution5-1. Table 3.6 shows the results of single bounce modeling.

Table 3.6: Single bounce model, synthetic scenario 72

scatterer	X_s (m)	Y_s (m)	Z_s (m)	*delay* (ns)	difference error				
					delay(%)	θ_{AoA}	θ_{AoD}	ϕ_{AoA}	ϕ_{AoD}
1	-0.9	0.8	0.3	70.44	0	0	0	0	0
2	-1.3	6.5	1.6	60.43	0	0	0	0	0
3	-1.1	8.5	1.7	60.47	0	0	0	0	0
4	-1.3	10.5	1.8	60.35	0	0	0	0	0
5	-0.8	11.5	1.2	60.75	0	0	0	0	0
6	-0.3	20	2.2	69.06	0	0	0	0	0
7	-1.6	21	0.3	71.03	0	0	0	0	0
8	-1.6	0.3	0.5	71.37	0	0	0	0	0
9	-3.2	0.8	2.5	67.34	0	0	0	0	0
10	-2.7	6	2	60.4	0	0	0	0	0
11	-2.7	8	2	60.36	0	0	0	0	0
12	-3.5	11.5	0.8	61.22	0	0	0	0	0
13	-3.2	20.5	1.9	69.48	0	0	0	0	0

When we look at Table 3.6, the method finds the locations of scatterers exactly since they are all single bounce cases (All % errors are zero).

Table 3.7: Double bounce model, synthetic scenario 72

scatterer		X_s	Y_s	Z_s	*delay*	difference error				
1^{st}	2^{nd}	(m)	(m)	(m)	(ns)	*delay*(%)	θ_{AoA}	θ_{AoD}	ϕ_{AoA}	ϕ_{AoD}
3	2	-1.07	8.13	2.02	60.56	0.08	5.51	1.49	0	0.01
5	3	-0.75	11.2	1.1	60.77	0.09	2.13	0.73	0	0.02
5	2	-0.7	10.78	1.26	60.77	0.1	1.59	0.3	0	0.05
11	10	-2.79	6.56	1.45	60.43	0.19	5.64	2.96	0	0
12	10	-3.54	11.4	1.02	61.31	0.26	3.49	1.58	0	0.14
12	13	-3.7	28.46	1.29	120.85	0.3	0.94	3.23	0	0.14
5	9	1.68	3.65	1.62	68.46	0.32	13.29	0.78	0	4.56
11	9	-3.14	0.83	2.58	67.34	0.42	3.69	0.14	0	0.02
6	4	-0.54	20.31	1.17	69.14	0.74	0.26	28.32	0	12.7
13	12	-4.54	18.41	-1.54	70.32	0.86	4.23	17.4	0	14.56
6	5	0.15	19.41	-0.19	69.48	0.86	1.64	26.85	0	13.85
4	2	-1.1	7.91	3.15	60.55	1.02	13.37	5.42	0	0.02
5	4	-1.06	13.54	0.77	61.34	1.04	4.04	3.58	0	0.39
12	11	-3.25	13.11	1.16	61.57	1.22	2.96	2.8	0	0.44
6	2	0.43	18.89	-1.06	69.29	1.6	2.94	16.53	0	2.23
8	11	-1.13	-6.59	0.91	22.26	2	7.06	1.3	0	0.72
10	9	-2.98	0.93	2.43	67.36	2.01	1.9	0.15	0	0.06
4	1	-0.59	0.6	2.95	70.91	2.06	11.93	0.8	0	0.19
6	3	0.27	19.19	0.46	69.21	2.29	1.03	42.65	0	8.6
3	1	-0.53	0.56	2.35	70.92	2.3	31.44	0.44	0	0.23
13	11	-3.92	19.35	1.38	69.53	4.4	0.31	18.84	0	35.28
13	10	-4.6	18.23	0.92	69.59	4.75	0.9	31.59	0	13.76
4	5	-1.04	9.47	5.01	68.21	5.61	24.82	16.64	0	1
4	9	-0.27	2.51	2.61	67.92	5.86	0.55	0.31	0	1.37
2	1	-0.98	0.85	1.96	70.93	6.19	41.29	0.31	0	0.06
3	9	-0.16	2.57	2.3	68.28	6.23	8.26	0.73	0	1.53
5	1	0.38	-0.01	1.5	70.73	6.51	41.08	0.04	0	1.58
2	7	-1.3	35.52	3.89	22.67	6.7	8.53	7.58	0	0.59
8	10	-1.28	-3.11	0.81	99.24	7.56	13.9	1.02	0	0.62
12	1	-8.62	5.71	0.52	71.84	8.31	44.13	0.38	0	15.01
2	9	-0.82	2.19	2.03	68.37	8.48	19.37	0.76	0	0.8
2	8	-1.11	-1.18	1.97	71.79	9.41	48.30	0.05	0	0.61
8	1	-1.55	1.22	0.47	74.94	10.14	16.91	0.16	0	0.21
1	9	-0.53	2.36	-0.64	77.77	11.35	21.85	3.31	0	1.53
11	1	-3.5	2.46	2.93	71.89	11.4	13.63	1.47	0	1.56
7	2	-0.15	14.72	-0.22	71.2	11.73	2.81	10.83	0	6.25
1	8	-1.03	-1.41	0.28	72.76	12.74	21.46	0.16	0	0.71

scatterer		X_s	Y_s	Z_s	*delay*	difference error				
1^{st}	2^{nd}	(m)	(m)	(m)	(ns)	*delay*(%)	θ_{AoA}	θ_{AoD}	ϕ_{AoA}	ϕ_{AoD}
7	5	-0.31	15.55	0.19	71.37	12.76	2.25	13.59	0	8.17
7	3	-0.24	15.21	0.58	71.25	13.04	2.25	19.06	0	7.39
10	1	-3.26	2.3	2.63	72.34	13.13	20.66	1.17	0	1.23
8	9	-1.5	1.79	-0.03	77.41	13.25	5.64	1.84	0	0.41
7	4	-0.76	17.49	1.1	71.18	13.61	1.09	26.81	0	16.79
11	8	-3.97	7.4	2.94	72.29	13.93	29.2	4.05	0	5.76
10	8	-3.57	6.21	2.63	72.5	15.14	31.24	2.73	0	3.76
7	6	-0.5	17.83	2.16	75.97	16.95	0.17	38.34	0	27.06
1	7	-1.11	44.72	-0.25	195.21	17.09	2.48	0.7	0	1.35
7	9	5.61	5.94	8.11	78.3	17.72	25.23	41.15	0	14.36
4	8	-0.83	-2	2.98	71.83	17.79	24.74	0.18	0	1.34
3	4	-1.12	12.78	1.61	73.71	17.97	0.32	1.52	0	2.76
10	11	-2.77	8.65	1.76	73.67	18.03	1.69	0.25	0	1.09
2	3	-1.16	8	1.68	73.76	18.06	0.51	0.75	0	1.07
3	8	-0.79	-2.14	2.37	71.87	18.49	34.05	0.01	0	1.47
12	9	-5.09	-0.3	0.12	67.95	18.96	39.5	1.09	0	1.75
3	7	-1.29	35.9	6.09	144.18	19.74	12.14	13.6	0	2.21
9	8	-4.32	8.47	2.95	78.69	20.31	30.06	5.22	0	8.22
9	1	-3.81	2.65	3.01	81.23	20.71	14.69	2.19	0	2.44

Table 3.8: Triple bounce model, synthetic scenario 72

scatterer			X_s	Y_s	Z_s	*delay*	difference error				
1^{st}	2^{nd}	3^{rd}	(m)	(m)	(m)	(ns)	*delay*(%)	θ_{AoA}	θ_{AoD}	ϕ_{AoA}	ϕ_{AoD}
4	3	2	-1.10	7.92	3.15	60.62	0.92	15.4	5.44	0	0.01
12	11	10	-3.55	11.44	1.02	61.33	0.77	3.46	1.57	0	0.26

In Table 3.4, estimated locations of scatterers are given with the increasing order of percentage delay error. There are 156 different cases but only a portion of them is shown in table. As percentage delay error increases, estimation of locations gets worse as expected. Also triple bounce cases are shown in Table 3.8. For triple bounces, only scatterers which are close to each other are chosen. Hence, reasonable locations are estimated using single bounce model with small percentage delay errors. By looking at Tables 3.4 and 3.8, estimated coordinates of scatterers are investigated and cases which have percentage delay error below seven are considered to be reasonable ones. Beyond seven percentage delay error, most of the cases can not be modeled with reasonable locations of single scatterers. For illustration purposes, some examples with different delay errors are given below.

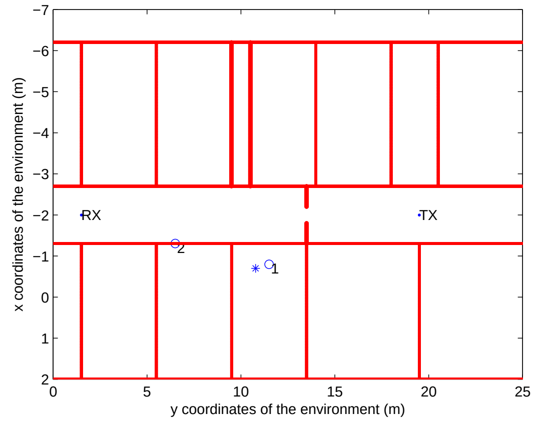

Figure 3.17: Single bounce model, scenario 72, 0.1 % delay error

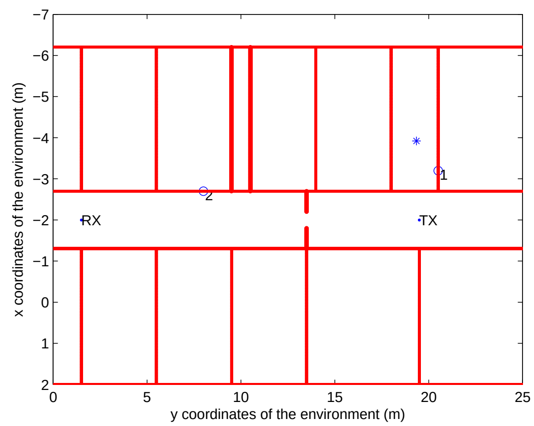

Figure 3.18: Single bounce model, scenario 72, 4.4 % delay error

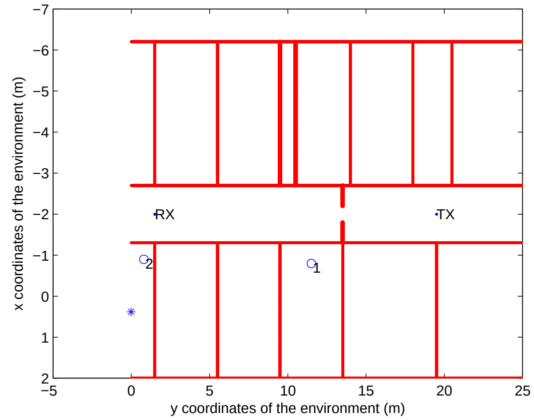

Figure 3.19: Single bounce model, scenario 72, 6.51 % delay error

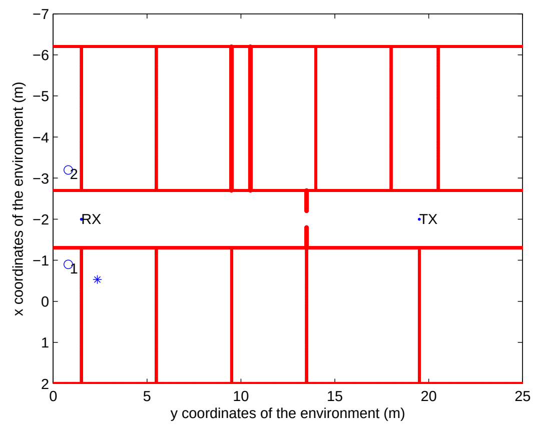

Figure 3.20: Single bounce model, scenario 72, 11.35 % delay error

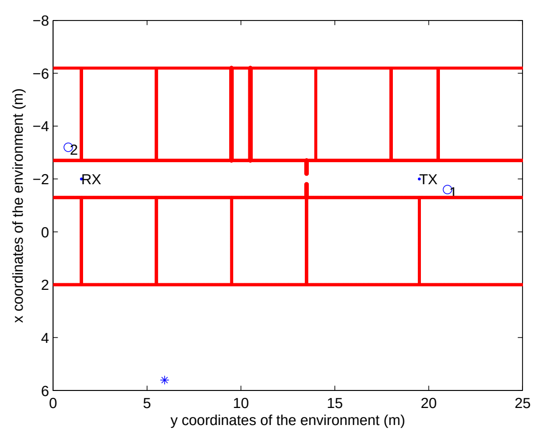

Figure 3.21: Single bounce model, scenario 72, 17.72 % delay error

where each '$\circ$' represents a synthetically placed scatterer and each '$*$' represents the estimated position for the single bounce model. Figures 3.17, 3.18 and 3.19 represent the cases which can be modeled with single bounce model. Estimated locations are close to both of the scatterers. Figures 3.20 and 3.21 represent the cases which are considered not to be modeled with single bounce model.

Results of synthetic scenarios 72 and 68 show that for small percentage delay errors, single bounce model locations are in the neighbourhood of first and second scatterer (close to locations of both scatterers or approximately on the intersection point of the incident wave coming towards the first scatterer and the scattered wave coming from the second scatterer). Estimated coordinates which are out of the error range are not physically close to those points. So we can not include those situations to the single bounce model. For more accuracy, we need to use a multi bounce model which is much more complicated than the single bounce model. Also waves which come through the multi bounce are not generally strong signals since they loose most of the energy during bouncings. Single and double bounce signals are stronger than remaining multi-bounced signals.

For both scenarios, common percentage delay error criterion is approximately 7. This percentage delay error is used to model the real scenarios.

3.5 Geometric Representation of Scatterer Locations

In order to find the locations of scatterers, we apply Solution5-1 to two different scenarios: Scenario 68 (room to corridor) and Scenario 72 (corridor to corridor). Seven percentage delay error is used for the scenarios. Since the number of multipaths within the desired delay error range is close to each other for all cycles, one cycle is chosen from each scenario. Results of other scenarios are not different from these results, so other scenarios are not illustrated here. Average number of multipaths is 6.13 for scenario 72 and 16.44 for scenario 68. Cycle 13 is used to generate results for scenario 68.

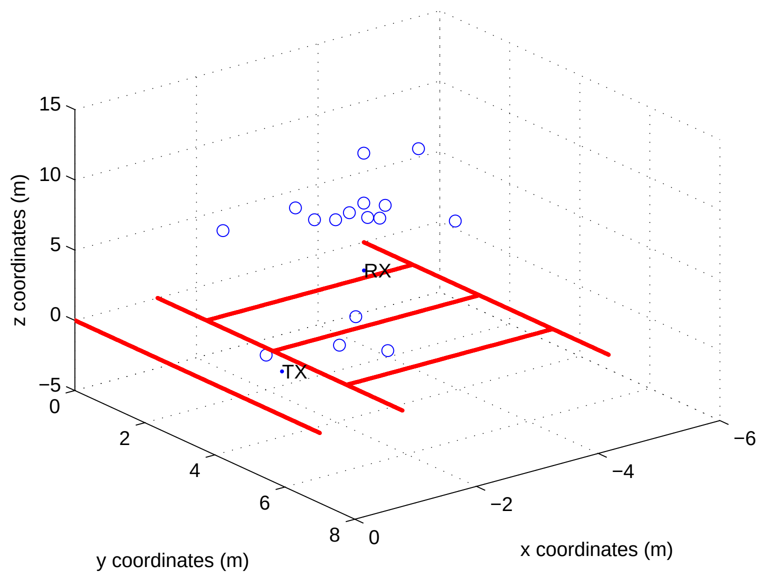

Figure 3.22: Scenario 68, cycle 13, xyz aspect

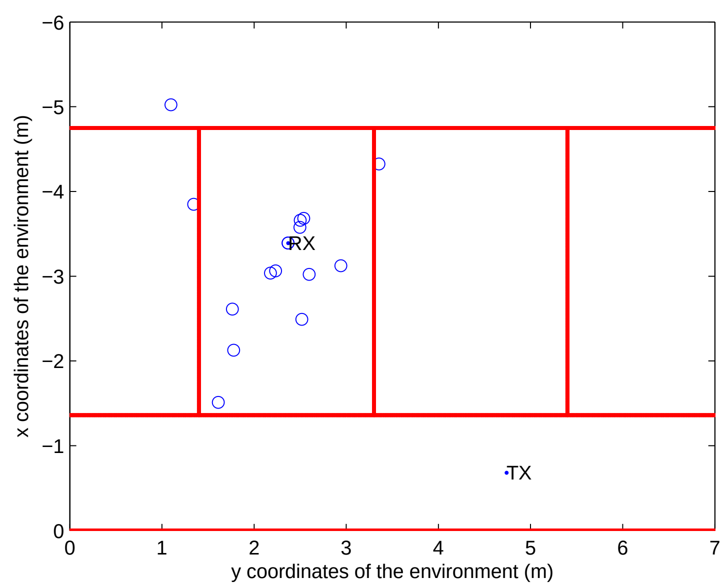

Figure 3.23: Scenario 68, cycle 13, xy aspect

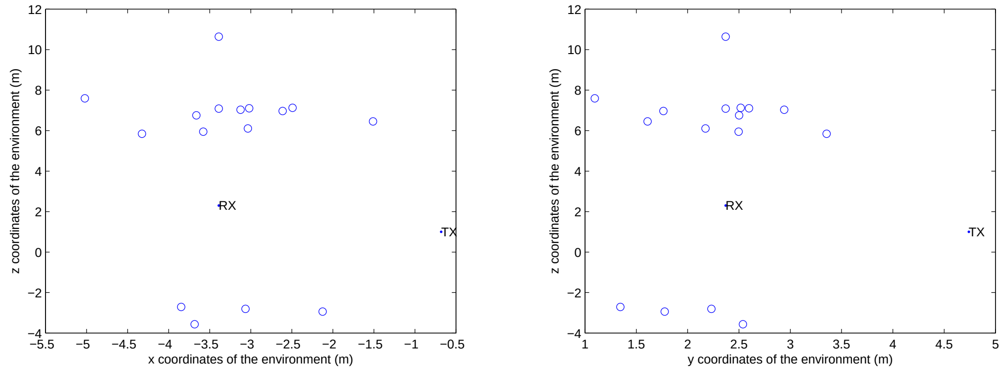

Figure 3.24: Scenario 68, cycle 13, xz and yz aspects respectively

where each '○' represents a scatterer. 16 Scatterers are found in the environment. Estimated locations of scatterers are shown from different views in Figures 3.22, 3.23 and 3.24 and reasonable locations for each MPC are found. Cycle 7 is used to generate results for scenario 72.

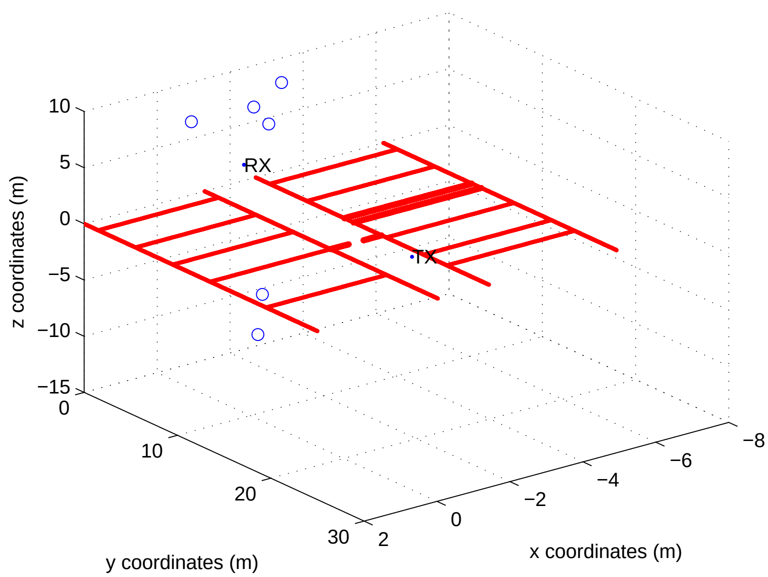

Figure 3.25: Scenario 72, cycle 7, xyz aspect

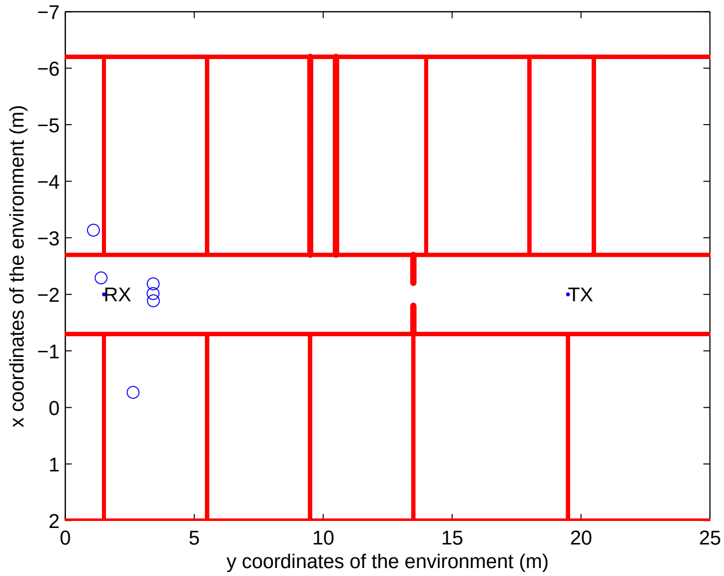

Figure 3.26: Scenario 72, cycle 7, xy aspect

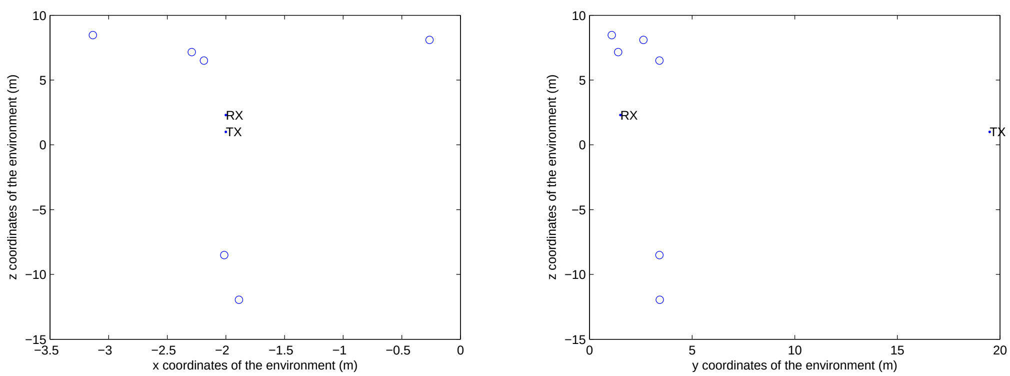

Figure 3.27: Scenario 72, cycle 7, xz and yz aspects respectively

where each '$\circ$' represents a scatterer. Six scatterers are found in the environment. Estimated locations of scatterers are found and shown from different aspects in Figures 3.25, 3.26 and 3.27. Most of the models in the literature do not include detailed physical models. Instead, a parametrized statistical model is used, where parameters are modeled with appropriate distributions. So it is important for us to know the physical locations. Since locations are known, the next step is to determine the electrical and physical properties of the scatterers.

3.6 Shapes and Electrical Properties of Scatterers

Measurement results demonstrated that the polarization diversity can provide considerable gain to a MIMO system in terms of space required and performance improvement [14]. In [7], the polarization is included and scatterers are modeled with spheres and cylinders. Scattering of each body is calculated. However this calculation increases the complexity of the electromagnetic channel. Hence, most of the channel models in the literature are based on statistical parameters. They are not interested in exact locations, polarization and characteristics of the scatterers because of the complexity of modeling.

In this work, we propose a geometric channel model which includes polarization in a simple way. In the model, each path corresponds to a bounce from a scatterer. For this purpose, discs of different sizes are placed to the locations of scatterers. For simplicity, we use PO approximation for the scattering. PO gives us the flexibility since incidence angle does not have to be equal to the reflection angle and allows us to include the size of the scatterer. In this sense, PO is an appropriate method for our channel model.

3.6.1 Physical Optics

Physical optics is a more general technique than geometric optics since at high frequencies, physical optics fields reduces to geometric optics in the specular direction [15], [16]. According to PO technique, when a wave is incident on a body, it produces surface currents. Induced surface current density is given by the geometric optics field. Scattered field is calculated by the integration of these surface currents and given by

$$\bar{J} = \hat{n} \times \bar{H}_{total}. \tag{3.32}$$

where $\hat{n}$ is the unit normal vector and $\bar{H}_{total}$ is the magnetic field on the surface. This current is used in the radiation integral to find the scattered field. We need to find the vector potential

$$\bar{A} = \int_S \int \frac{\bar{J}e^{-jkR}}{4\pi R} ds \tag{3.33}$$

where R is the distance between the source and the observation point. From geometric optics, tangential component of the magnetic field is twice the incident magnetic field. So physical optic current becomes:

$$\bar{J}_s = 2\hat{n} \times \bar{H}^i \tag{3.34}$$

where $\bar{H}_i$ is the incident magnetic field vector. Far zone scattered field is given by $\bar{E}_s = -jw\mu\bar{A}$ where w is the radial frequency, μ is permeability and we can write the scattered field as:

$$\bar{E}^s = -\frac{jw\mu e^{-jkr}}{4\pi r} \int_S \int 2(\hat{n} \times H^i) e^{-jkr_s} ds \tag{3.35}$$

where r is the distance from phase reference plane to the scatterer and r_s is the distance from the phase reference plane to the far field observation point.

3.6.2 Reflection Coefficients for Impedance Surfaces

Let the surface impedance be z.

$$z = j\eta \tan(kd) \tag{3.36}$$

where η is the intrinsic impedance of the material, k is the propagation constant in the layer and d is the thickness of the coating layer. Using equalities below:

$$\eta = \sqrt{\frac{\mu}{\epsilon}} = \frac{w\mu}{k} = \eta_0 \sqrt{\frac{\mu_r}{\epsilon_r}} \tag{3.37}$$

$$k = w\sqrt{\mu\epsilon}, \qquad k_0 = w\sqrt{\mu_0\epsilon_0}, \qquad k = k_0\sqrt{\mu_r\epsilon_r} \tag{3.38}$$

where μ is the absolute permeability, ϵ is the absolute permittivity, η_0 is the intrinsic impedance of free space, k_0 is the propagation constant in free space,

ϵ_0 is the permittivity of free space, μ_0 is the permeability of free space, ϵ_r is the dielectric constant of the medium (relative permittivity) and μ_r is the relative permeability. There are two kinds of polarizations:

Parallel Polarization :

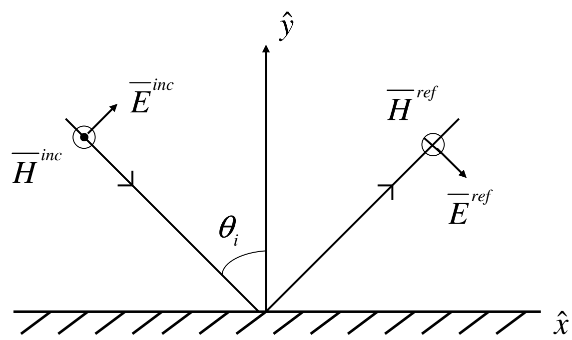

Figure 3.28: Parallel polarization

$$\bar{E}^{inc} = E_0(\cos\theta^i \hat{a}_x + \sin\theta^i \hat{a}_y)e^{-jkx\sin\theta^i + jky\cos\theta^i} \tag{3.39}$$

$$\bar{H}^{inc} = \hat{a}_z \frac{E_0}{\eta_0} e^{-jkx\sin\theta^i + jky\cos\theta^i} \tag{3.40}$$

$$\bar{E}^{ref} = E_{ref}(\cos\theta^i \hat{a}_x - \sin\theta^i \hat{a}_y)e^{-jkx\sin\theta^i - jky\cos\theta^i} \tag{3.41}$$

$$\bar{H}^{ref} = -\hat{a}_z \frac{E_{ref}}{\eta_0} e^{-jkx\sin\theta^i - jky\cos\theta^i} \tag{3.42}$$

where $\bar{E}^{inc}$ and $\bar{H}^{inc}$ are the incident electric and the magnetic fields, respectively; $\bar{E}^{ref}$ and $\bar{H}^{ref}$ are the reflected electric and the magnetic fields, respectively; η_0 is the intrinsic impedance of free space, E_0 is the amplitude of the incident electric field and θ^i is the angle of incidence.

Boundary conditions:

$$\bar{J} = \sigma\bar{E} \rightarrow \bar{E} = R\bar{J} \rightarrow \bar{E}_{tan} = Z\hat{n} \times \bar{H} \tag{3.43}$$

where $\bar{J}$ is the current vector, σ is the conductivity, at y=0

$$\cos\theta^i E_0 e^{-jkx\sin\theta^i} + \cos\theta^i E^{ref} e^{-jkx\sin\theta^i} = z\hat{a}_y \times [\hat{a}_z \frac{E_0}{\eta_0} - \hat{a}_z \frac{E^{ref}}{\eta_0}] e^{-jkx\sin\theta^i} \tag{3.44}$$

$$(\frac{z}{\eta_0} + \cos\theta^i)E^{ref} = (\frac{z}{\eta_0} - \cos\theta^i)E_0 \tag{3.45}$$

we obtain the reflection coefficient for parallel polarization as:

$$R_{//} = \frac{E^{ref}}{E_0} = \frac{\frac{z}{\eta_0} - \cos\theta^i}{\frac{z}{\eta_0} + \cos\theta^i} \tag{3.46}$$

Perpendicular Polarization :

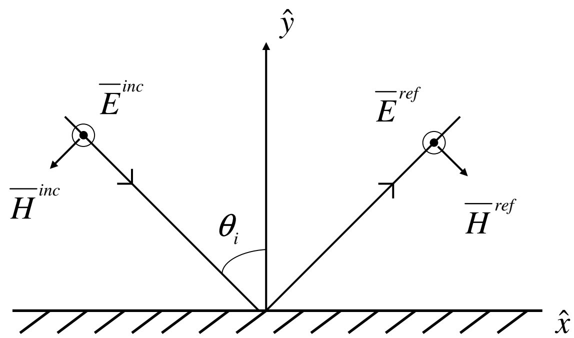

Figure 3.29: Perpendicular polarization

$$\bar{E}^{inc} = \hat{a}_z E_0 e^{-jkx\sin\theta^i + jky\cos\theta^i} \tag{3.47}$$

$$\bar{H}^{inc} = (-\cos\theta^i \hat{a}_x - \sin\theta^i \hat{a}_y)\frac{E_0}{\eta_0} e^{-jkx\sin\theta^i + jky\cos\theta^i} \tag{3.48}$$

$$\bar{E}^{ref} = \hat{a}_z E_{ref} e^{-jkx\sin\theta^i - jky\cos\theta^i} \tag{3.49}$$

$$\bar{H}^{ref} = (\cos\theta^i \hat{a}_x - \sin\theta^i \hat{a}_y)\frac{E_{ref}}{\eta_0} e^{-jkx\sin\theta^i - jky\cos\theta^i} \tag{3.50}$$

Boundary conditions at y=0:

$$E_0 + E^{ref} = z(-\frac{E_0}{\eta_0}\cos\theta^i + \frac{E^{ref}}{\eta_0}\cos\theta^i) \tag{3.51}$$

$$E^{ref}(\frac{z}{\eta_0}\cos\theta^i - 1) = E_0(\frac{z}{\eta_0}\cos\theta^i + 1) \tag{3.52}$$

we obtain reflection coefficient for perpendicular polarization as:

$$R_{\perp} = \frac{E^{ref}}{E_0} = \frac{\frac{z}{\eta_0}\cos\theta^i - 1}{\frac{z}{\eta_0}\cos\theta^i + 1} \tag{3.53}$$

3.6.3 PO Solution for Impedance Disc

Disc is placed in x-y coordinates and its normal is in z direction of local coordinates. Angles are defined as shown in Figure 3.30.

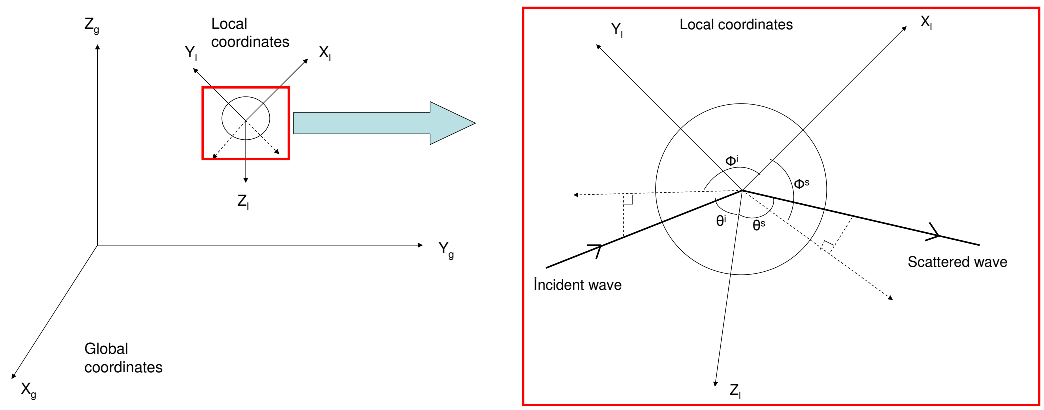

Figure 3.30: Location of disc shown in local and global coordinates

Since there are several scatterers in the environment where each is described in its own local coordinate, we need to express the results in global coordinates.

Total electric field is

$$\bar{E}^i = \hat{a}_\theta \bar{E}^i_\theta + \hat{a}_\phi \bar{E}^i_\phi \tag{3.54}$$

Using the Equation 3.34, we obtain PO surface current as:

$$\bar{J}_s = \frac{e^{j\hat{k}_i r}}{\eta_0}[(1-R_\parallel)E^i_\phi(\hat{a}_x \cos\theta^i \sin\phi^i + \hat{a}_y \cos\theta^i \cos\phi^i) + (1-R_\perp)E^i_\theta(\hat{a}_x \cos\phi^i + \hat{a}_y \sin\phi^i)] \tag{3.55}$$

Scattered field is obtained as

$$E^s_\theta = \frac{-jw\mu}{4\pi r}e^{-jkr}\int_S\int (J_x \cos\theta^s \cos\phi^s + J_y \cos\theta^s \sin\phi^s - J_z \sin\theta^s)e^{jk\rho}ds' \tag{3.56}$$

and

$$E^s_\phi = \frac{jw\mu}{4\pi r}e^{-jkr}\int_S\int (J_x \sin\phi^s - J_y \cos\phi^s)e^{jk\rho}ds' \tag{3.57}$$

where

$$\rho = x' \sin\theta^s \cos\phi^s + y' \sin\theta^s \sin\phi^s + z' \cos\theta^s \tag{3.58}$$

It can be written in a more compact way as follows:

$$\begin{bmatrix} E_\theta^s \\ E_\phi^s \end{bmatrix} = \bar{\bar{\alpha}} \begin{bmatrix} E_\theta^i \\ E_\phi^i \end{bmatrix} \frac{I_0}{\eta_0} \frac{jw\mu}{4\pi r} e^{-jkr} \tag{3.59}$$

where

$$\bar{\bar{\alpha}} = \begin{bmatrix} -\cos\theta^s \cos(\phi^s - \phi^i)(1 - R_\perp) & -\cos\theta^i \cos\theta^s \sin(\phi^s - \phi^i)(1 - R_\parallel) \\ \sin(\phi^s - \phi^i)(1 - R_\perp) & -\cos\theta^i \cos(\phi^s - \phi^i)(1 - R_\parallel) \end{bmatrix} \tag{3.60}$$

where θ^i and ϕ^i are the elevation and azimuth angles of incident wave in local coordinates; θ^s and ϕ^s are the elevation and azimuth angles of scattered wave in local coordinates.

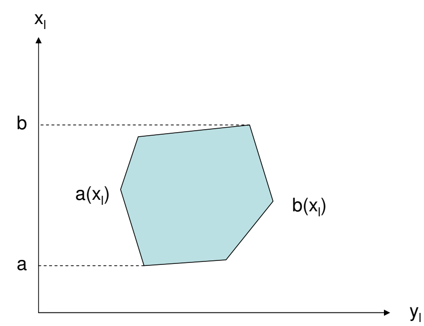

Figure 3.31: Integral over the surface of the plane

From Figure 3.31 integral is computed as:

$$I_0 = \int_{x_l=a}^{b} \int_{y_l=a(x_l)}^{b(x_l)} e^{ux_l+vy_l} dx_l dy_l \tag{3.61}$$

where

$$\begin{aligned} u &= k(\sin\theta^i \cos\phi^i + \sin\theta^s \cos\phi^s) \\ v &= k(\sin\theta^i \sin\phi^i + \sin\theta^s \sin\phi^s) \end{aligned} \tag{3.62}$$

From $\bar{\alpha}$ matrix, scattering coefficients become :

$$\alpha_{vv} = -\cos\theta^s \cos(\phi^s - \phi^i)(1 - R_\perp) \tag{3.63}$$

$$\alpha_{vh} = -\cos\theta^i \cos\theta^s \sin(\phi^s - \phi_i)(1 - R_\parallel) \tag{3.64}$$

$$\alpha_{hv} = \sin(\phi^s - \phi_i)(1 - R_{\perp}) \tag{3.65}$$

$$\alpha_{hh} = -\cos\theta^i \cos(\phi^s - \phi^i)(1 - R_{\parallel}) \tag{3.66}$$

[17]

In the case of the disc, Equation 3.61 turns into:

$$I_0 = \int_{r=0}^{r=a} \int_{\phi=0}^{\phi=2\pi} e^{j(ur\cos\phi + vr\sin\phi)} r dr d\phi \tag{3.67}$$

where a is the radius of disc. A detailed calculation is done and using the property of bessel function $J_0(z) = \frac{1}{\pi}\int_0^{\pi} e^{\mp z\cos\theta} d\theta$, I_0 turns into

$$I_0 = \frac{2\pi a \cos\left(\arctan\frac{v}{u}\right)}{ju} \tag{3.68}$$

In the case of small disc area, I_0 can be taken as the area of the disc. For our case I_0 is taken as :

$$I_0 = \pi a^2 \tag{3.69}$$

3.7 Orientation and Dielectric Properties of Scatterers

Calculating the electrical and geometrical parameters of aforementioned discs to model the scatterers allows an accurate analysis of features of the scattering environment. Among those features, the orientation of the scattering objects and the impact of different dielectric properties can be examined. For this purpose θ^i, θ^s and $\phi^s - \phi^i$ must be known. Since scattering coefficients (α_{vv}, α_{vh}, α_{hv}, α_{hh}) are given in measurement data, these parameters can be found using Equations 3.63, 3.64, 3.65 and 3.66. Using these parameters, orientation of scatterers can be found easily.

As seen from Equations 3.63, 3.64, 3.65 and 3.66, phases of α_{vv} and α_{hv} are equal to each other since they are multiplied with same reflection coefficient.

Similarly, phases of α_{vh} and α_{hh} are equal to each other. They are dependent to each other. But in real scattering environment they are independent numbers. Hence, we can not directly make a one-to-one correspondence between calculated and measured values of these four parameters. Instead, tolerating some difference error between actual and calculated values, a brute force search for α_{vv}, α_{vh}, α_{hv} and α_{hh} is done. For this purpose, a four dimensional table (θ^i, θ^s, $\phi^i - \phi^s$, ϵ_r) is formed. θ^i and θ^s are taken between $0\,^\circ$ and $90\,^\circ$ with $5\,^\circ$ resolution, $\phi^i - \phi^s$ is taken between $0\,^\circ$ and $360\,^\circ$ with $5\,^\circ$ resolution and ϵ_r is taken between 2 and 5 with 0.05 resolution. μ_r is taken to be 1.

There are 19x19x73x61=1,607,533 possibilities. For each case α_{vv}, α_{vh}, α_{hv} and α_{hh} are calculated by using Equations 3.63, 3.64, 3.65 and 3.66. As a result, we have 1,607,533 different $\bar{\alpha}$ matrices. For each case, difference error is calculated and the minimum of all calculated difference errors is taken. Difference error is defined as:

$$error_{diff}(\%) = \frac{(\alpha^c_{vv} - \alpha^m_{vv})^2 + (\alpha^c_{vh} - \alpha^m_{vh})^2 + (\alpha^c_{hv} - \alpha^m_{hv})^2 + (\alpha^c_{hh} - \alpha^m_{hh})^2}{(\alpha^m_{vv})^2 + (\alpha^m_{vh})^2 + (\alpha^m_{hv})^2 + (\alpha^m_{hh})^2} \times 100 \tag{3.70}$$

where α^c_{vv}, α^c_{vh}, α^c_{hv} and α^c_{hh} are the calculated values tabulated in table; α^m_{vv}, α^m_{vh}, α^m_{hv} and α^m_{hh} are the values coming from measurement data.

Parameters giving the minimum difference error are assigned to that scatterer. Finally, θ^i, θ^s and $\phi^i - \phi^s$ are determined from the table.

Next step is to find the normal direction of discs. For that purpose, a simple geometry is constituted.

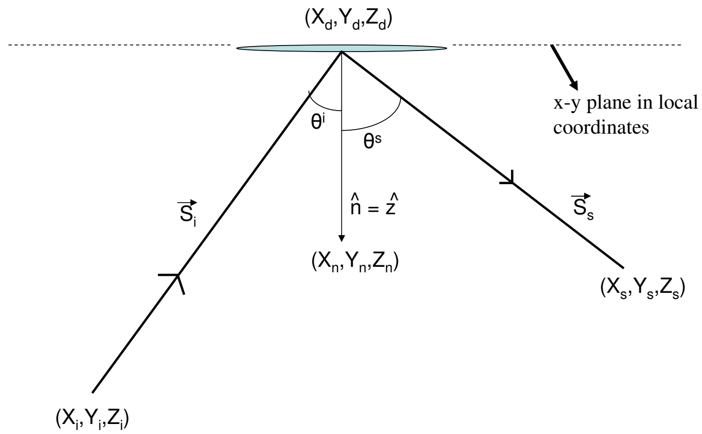

Figure 3.32: Simple geometry for calculation of disc's normal

All parameters are shown in Figure 3.32. (X_i,Y_i,Z_i) are coordinates of the transmitter, (X_s,Y_s,Z_s) are coordinates of the receiver and (X_d,Y_d,Z_d) are coordinates of the center of the disc. Directions of the incident and the scattered waves are known. Normal vector is denoted by $\hat{n}$ and (X_n,Y_n,Z_n) are chosen in the normal direction such that $|\hat{n}|$ is equal to 1 as denoted in Equation 3.74. Vectors are defined as:

$$\begin{aligned} \vec{S}_i &= (X_d - X_i, Y_d - Y_i, Z_d - Z_i) \\ \hat{n} &= (X_n - X_d, Y_n - Y_d, Z_n - Z_d) \\ \vec{S}_s &= (X_s - X_d, Y_s - Y_d, Z_s - Z_d) \end{aligned} \tag{3.71}$$

Scalar product rule and the unit vector property give us:

$$\begin{aligned} \vec{S}_i \cdot \hat{n} &= |\vec{S}_i||\hat{n}| \cos\theta^i \\ (X_d - X_i)(X_n - X_d) + (Y_d - Y_i)(Y_n - Y_d) + (Z_d - Z_i)(Z_n - Z_d) &= \\ \sqrt{(X_d - X_i)^2 + (Y_d - Y_i)^2 + (Z_d - Z_i)^2} \cos\theta^i, \end{aligned} \tag{3.72}$$

$$\begin{aligned} \vec{S}_s \cdot \hat{n} &= |\vec{S}_s||\hat{n}| \cos\theta^s \\ (X_n - X_d)(X_s - X_d) + (Y_n - Y_d)(Y_s - Y_d) + (Z_n - Z_d)(Z_s - Z_d) &= \\ \sqrt{(X_n - X_d)^2 + (Y_n - Y_d)^2 + (Z_n - Z_d)^2} \cos\theta^s \end{aligned} \tag{3.73}$$

and

$$\sqrt{(X_n - X_d)^2 + (Y_n - Y_d)^2 + (Z_n - Z_d)^2} = 1 \tag{3.74}$$

Since θ^i and θ^s are known, X_n, Y_n and Z_n are found from these 3 equations. In order to find the global location of normal vector, we need to find the angles seen from global coordinate axis. Angle between the normal direction and the global x-axis can be found as:

$$\theta^x = \arccos\left(X_n - X_d\right) \tag{3.75}$$

Similarly, angles between the normal direction and the global y-axis and the global z-axis can be found respectively:

$$\begin{aligned} \theta^y &= \arccos\left(Y_n - Y_d\right) \\ \theta^z &= \arccos\left(Z_n - Z_d\right) \end{aligned} \tag{3.76}$$

As a result, normal direction is found in global coordinates.

3.7.1 Sizes of the Discs

Using PO surface current integration, sizes of the discs are considered. Sizes depend on the power of that multipath since integration is taken over the disc area. Received power is calculated to find the size. From Figure 3.1, received power can be written as:

$$P_r = G_t P_t \frac{1}{4\pi d_1^2}|I_0|^2 \frac{1}{4\pi d_2^2}\frac{\lambda^2}{4\pi}G_r \qquad \xrightarrow{G_t = G_r = 1} \qquad \frac{P_r}{P_t} = \frac{\lambda^2 |I_0|^2}{(4\pi)^3 d_1^2 d_2^2} \tag{3.77}$$

where G_t is the transmitter gain (taken to be 1), G_r is the receiver gain (taken to be 1), P_t is the transmitted power, P_r is the received power and λ is the wavelength of plane wave in free space.

Scattering coefficients given in measurement data are modeled to be:

$$\frac{P_r}{P_t} = |\alpha|^2 \qquad \rightarrow \qquad |\alpha|^2 = \frac{\lambda^2 |I_0|^2}{(4\pi)^3 d_1^2 d_2^2} \tag{3.78}$$

where d_1, d_2 are the distances shown in Figure 3.1 and

$$|\alpha|^2 = |\alpha_{vv}|^2 + |\alpha_{vh}|^2 + |\alpha_{hv}|^2 + |\alpha_{hh}|^2 \qquad and \qquad I_0 = \pi a^2 \tag{3.79}$$

Hence radius of the disc "a" is found to be

$$a = [\frac{|\alpha|^2 (4\pi)^3 d_1^2 d_2^2}{\lambda^2 \pi^2}]^{\frac{1}{4}} \tag{3.80}$$

Finally, discs are placed to their coordinates with the obtained orientations, sizes and dielectric properties. So, the model is completed. Results for cycle 13 from scenario 68 and cycle 7 from scenario 72 are given in Tables 3.9 and 3.10, respectively.

Table 3.9: List of environment parameters in scenario 68

X_s (m)	Y_s (m)	Z_s (m)	θ^i (°)	θ^s (°)	$\phi^s - \phi^i$ (°)	ϵ_r	θ^x (°)	θ^y (°)	θ^z (°)	R_{disc} (cm)
-3.02	2.59	7.105	80	85	355	2	137.43	48.71	98.57	12.91
-1.51	1.61	6.46	50	15	345	2.1	75.95	48.03	134.647	9.53
-3.578	2.49	5.94	45	10	55	2.15	53.2	66.19	133.75	9.92
-3.84	1.34	-2.71	90	70	170	2.65	15.4	105.27	91.94	14.93
-3.06	2.23	-2.8	60	25	95	2.1	37.79	73.62	57.04	8.71
-3.123	2.94	7.03	90	80	195	2.35	29.61	119.59	89.38	17.14
-3.035	2.17	6.1	30	10	240	2.2	77.57	63.42	150.23	16.87
-3.39	2.37	10.63	30	35	105	2	89.02	81.46	171.4	12.74
-2.61	1.76	6.96	90	70	355	2.55	86.2	7.75	83.25	12.42
-2.49	2.52	7.13	90	60	340	2.2	66.16	24.64	95.91	10.03
-3.68	2.54	-3.56	30	10	240	2	69.03	68.68	30.67	9
-4.32	3.35	5.84	35	5	140	2.15	50.29	80.87	138.83	12.54
-2.125	1.77	-2.94	90	80	180	4.6	31.6	117.16	75.08	12.74
-3.39	2.37	7.09	0	0	300	2.15	48.82	138.82	90	14.72
-3.66	2.5	6.75	35	5	230	2.1	59.24	71.6	143.06	8.86
-5.02	1.09	7.59	15	5	80	2	61.39	69.59	143.67	11.88

Table 3.10: List of environment parameters in scenario 72

X_s (m)	Y_s (m)	Z_s (m)	θ^i (°)	θ^s (°)	$\phi^s - \phi^i$ (°)	ϵ_r	θ^x (°)	θ^y (°)	θ^z (°)	R_{disc} (cm)
-0.26	2.63	8.095	80	85	355	2	137.43	48.71	98.57	12.91
-2.29	1.39	7.153	50	15	345	2.1	75.95	48.03	134.65	9.53
-3.13	1.09	8.47	45	10	55	2.15	53.2	66.19	133.75	9.92
-2.01	3.41	6.507	90	70	170	2.65	15.4	105.27	91.94	14.93
-1.89	3.42	-11.95	60	25	95	2.1	37.79	73.62	57.04	8.71
-3.12	2.94	7.03	90	80	195	2.35	29.61	119.59	89.38	17.14

where R_{disc} is the radius of the disc placed. As seen from the tables, each disc is placed to a location (X_s, Y_s, Z_s) with given ϵ_r. The orientation of the disc is denoted by the angles (θ^x, θ^y, θ^z) and finally, the size of the disc is denoted by R_{disc}. So, each MPC is modeled with single bounce model without knowing the trace of the path traveled.

Chapter 4

Application of the Channel Model

4.1 Introduction

Polarization diversity has gained much attention recently since it can increase the system performance. The applicability of polarization diversity can be determined by analyzing cross-polarization discrimination (XPD) values. The XPD represents the power imbalance between the polarizations and is defined as the ratio of the copolarized signal power and the cross polarized signal power.

4.1.1 Definition of XPD

When a vertically polarized wave impinges upon a scatterer, both vertically and horizontally polarized waves are scattered from the scatterer; also when horizontally polarized wave impinges upon a scatterer, both vertically and horizontally polarized waves are scattered from the scatterer. This is illustrated in Figure 4.1.

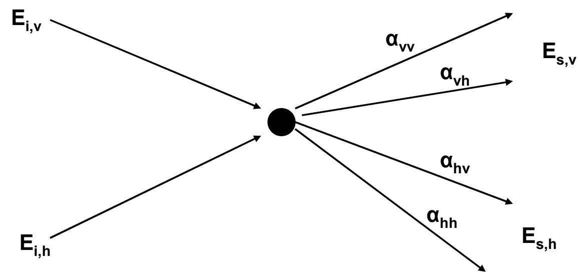

Figure 4.1: Representation of scattering coefficients

Hence, scatterers are modeled with 2x2 matrices and shown as:

$$\begin{bmatrix} \bar{E}_{s,v} \\ \bar{E}_{s,h} \end{bmatrix} = \begin{bmatrix} \alpha_{vv} & \alpha_{vh} \\ \alpha_{hv} & \alpha_{hh} \end{bmatrix} \begin{bmatrix} \bar{E}_{i,v} \\ \bar{E}_{i,h} \end{bmatrix} \tag{4.1}$$

If transmit antennas are vertically polarized, XPD ratio is calculated as:

$$XPD_v = \frac{|E_{s,v}|^2}{|E_{s,h}|^2} = \frac{\alpha_{vv}\alpha^*_{vv}|E_{i,v}|^2}{\alpha_{hv}\alpha^*_{hv}|E_{i,v}|^2} = \frac{|\alpha_{vv}|^2}{|\alpha_{hv}|^2} \tag{4.2}$$

where "$*$" denotes complex conjugate. In a similar manner, horizontally polarized XPD ratio is

$$XPD_h = \frac{|\alpha_{hh}|^2}{|\alpha_{vh}|^2} \tag{4.3}$$

If we express it in a general way, it is like:

$$XPD = \frac{\sum_{k=1}^{N} |\alpha^k_{vv}|^2 + |\alpha^k_{hh}|^2}{\sum_{k=1}^{N} |\alpha^k_{vh}|^2 + |\alpha^k_{hv}|^2} \tag{4.4}$$

where N is the number of multipaths and powers of vertically and horizontally incident fields are assumed to be equal.

4.2 Background

In literature, XPD and its relation to other channel parameters are studied. Indoor measurements show that hybrid polarization systems perform better than single polarized systems [4]. XPD values of vertical/horizontal polarization are larger than +45/-45 slanted polarization, XPD values are greater in LOS paths when compared to NLOS paths [18]. Relationships between XPD, signal cross correlation, and polarization diversity gain are examined experimentally in [19]. Another outdoor NLOS channel measurement shows that XPD decays with the increasing excess loss [20].

4.3 Related Study on Modeling XPD

In this paper, a model is presented for cross polarized channel. Using the model and the measurements partly, it discusses XPD and its dependence on distance. Distance is measured from the receiver to the point located in the direction such that distance from the point to the transmitter gets bigger. According to literature review and the model developed in [11], XPD increases as the distance increases and modeled in [11] as:

$$XPD(d)|_{dB} = XPD_{d_0=1m} + n_1 \cdot 10log_{10}(\frac{d}{d_0}) \tag{4.5}$$

where $2 \leq d \leq 50$ is the distance in meters and the constant parameters are given by the measurements

	$XPD_{d_0=1m}(dB)$	n_1
LOS	7.9	0.55
NLOS	2.6	0.29

This gives a result like below:

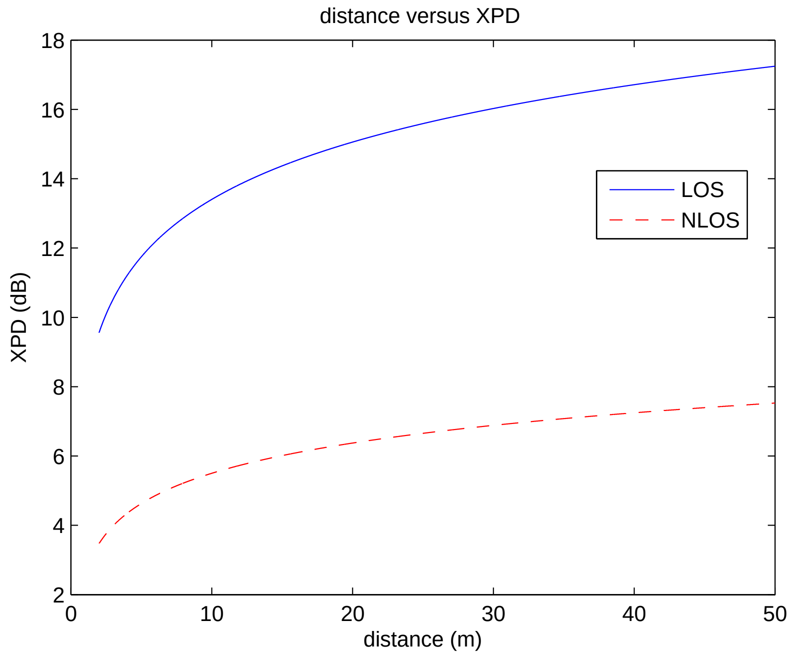

Figure 4.2: Distance dependent XPD in indoor environment

4.4 Work Done, Comparison and Contribution

In order to discuss XPD and its dependence on distance, we studied two different models: Ray tracing model and the geometric channel model developed in previous chapter.

4.4.1 Model Based on 2D Ray Tracing Algorithm

Two dimensional ray tracing algorithm is used for modeling.

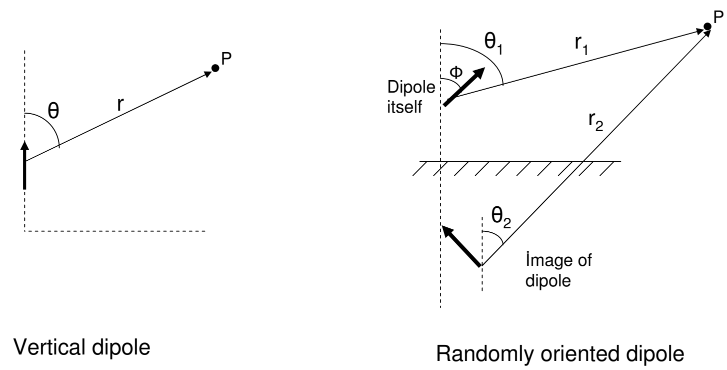

Figure 4.3: Vertically and randomly oriented dipole geometry

Direct electric field received at the observation point is shown in Figure 4.3 and formulated as:

$$E_\theta^d = j\eta RkI_0 l\frac{e^{-jkr}}{4\pi r}\sin\theta\hat{a}_\theta \tag{4.6}$$

where the reflection coefficient $R = 1$ for direct path, I_0 is the current flowing through dipole, k is the propagation constant, l is the length of the dipole and r is the distance between dipole and the observation point. For a randomly oriented dipole, parameters are shown in Figure 4.3 and formulation turns into:

$$E_\theta^d = j\eta kI_0 l\frac{e^{-jkr_1}}{4\pi r_1}\sin\theta_1(\hat{a}_x\sin\phi + \hat{a}_y\cos\phi)\cdot\hat{a}_\theta \tag{4.7}$$

$$E_\theta^r = j\eta RkI_0 l\frac{e^{-jkr_2}}{4\pi r_2}\sin\theta_2(-\hat{a}_x\sin\phi + \hat{a}_y\cos\phi)\cdot\hat{a}_\theta \tag{4.8}$$

$$E_{total} = E_\theta^d + E_\theta^r \tag{4.9}$$

where E_θ^r is the reflected E-field. Reflection coefficient is:

$$R = \frac{\eta_1 - \eta_2}{\eta_1 + \eta_2} \tag{4.10}$$

where η_1 is the intrinsic impedance of the propagating environment and η_2 is the intrinsic impedance of the reflecting medium.

XPD is studied in a tunnel environment. Diffractions are not included in the model. Instead, multiple reflections and image theory are used in modeling. Environment is shown in Figure 4.4.

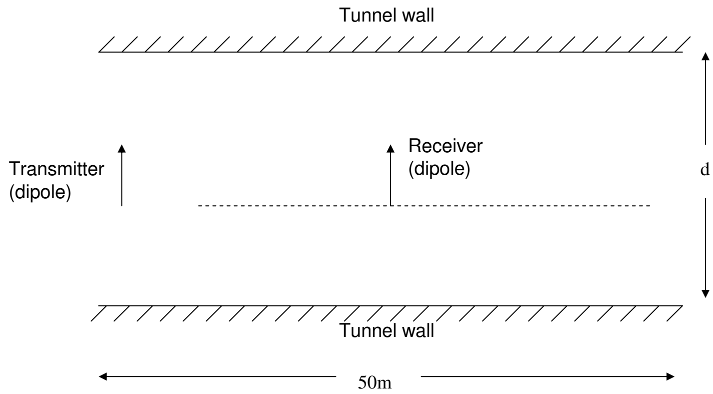

Figure 4.4: Tunnel environment where TX and RX are placed

where d is the width of the tunnel and receiver location is changed gradually over dashed line shown in Figure 4.4. For every point on dashed line, XPD is calculated each time and we tried to fit the known curve to our result. Slope of the curve depends on the frequency, maximum number of reflections (if it is 2, it includes 1 and 2 reflections; if it is 3, it includes 1,2 and 3 reflections and so on), whether environment is LOS or NLOS and the intrinsic impedance of the walls. The result is depicted in Figure 4.5.

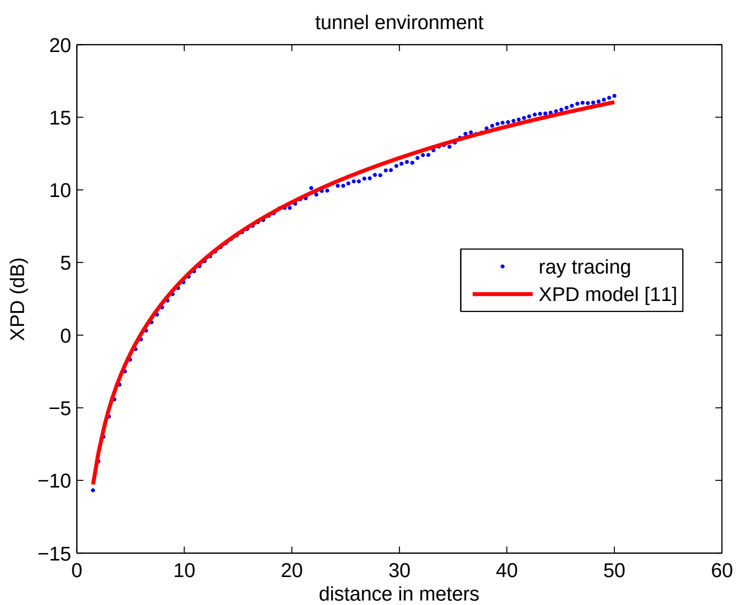

Figure 4.5: Comparison of ray tracing model and model in [11]

In the simulations frequency is 300MHz, the maximum number of reflections is 2, d is 20m and the intrinsic impedance of the wall is 200Ω. Curve represented with solid line is fitted to the curve with dashed line. Solid line is obtained by using Equation 4.5 with $XPD_{d_0=1m}$ is -10.68dB and n_1 is 1.73. General behaviour of XPD is same as the behaviour represented in [11]. Same formula can be used with different values of $XPD_{d_0=1m}$ and n_1. Table 4.1 shows formula constants calculated according to different environment parameters.

Table 4.1: Formula constants versus environment parameters

$\#ofreflections$	$Frequency$ (MHz)	$intrinsicimpedance$ (Ω)	$XPD_{d_0=1m}$ (dB)	n_1
2	3000	0	-10.375	1.73
2	3000	200	-10.303	1.74
2	3000	300	-10.275	1.76
4	300	200	-10.675	1.74
4	1000	200	-10.696	1.73
4	3000	200	-10.299	1.73
1	300	200	-10.683	1.75
2	300	200	-10.675	1.74
3	300	200	-10.675	1.74

As a result, our work supports the idea presented in [11] and hence, XPD increases as distance increases.

4.4.2 XPD Properties of Our Model

XPD ratio depends on scattering coefficients and scattering coefficients in our model depend on the values of θ^i, θ^s, $\phi^s - \phi^i$ and ϵ_r.

XPD Behaviour of Geometric Channel Model

In this section 1^{st} cycle of scenario 68 is used. Other scenario and cycle results are not different. Using our model, locations of scatterers are calculated with Solution5-1. Discs are placed to those locations with calculated normal directions, electrical properties and orientations using the procedure explained in previous chapter. So, a deterministic scenario is formed. After that, receiver antenna location is changed gradually in the direction shown in Figure 4.6 .

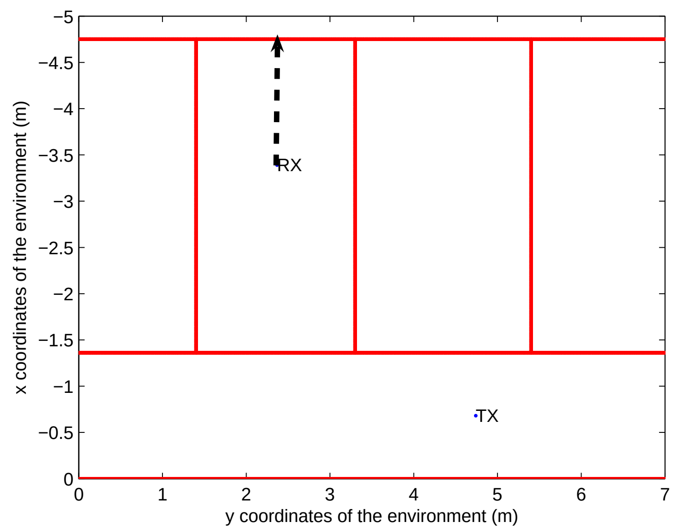

Figure 4.6: XPD variation in scenario 68

As the location of RX changes, scattering coefficient parameters (θ^i, θ^s, $\phi^s - \phi^i$) also change. So, for each new receiver antenna location, scattering coefficient parameters are calculated using the geometrical relationship between TX, RX and the scatterer. Using these parameters, scattering coefficients are calculated using Equations 3.63, 3.64, 3.65 and 3.66. Finally, XPD ratio is calculated. This procedure is applied for 2m $\leq d \leq$ 50m. XPD behaviour of channel with increasing distance is found to be:

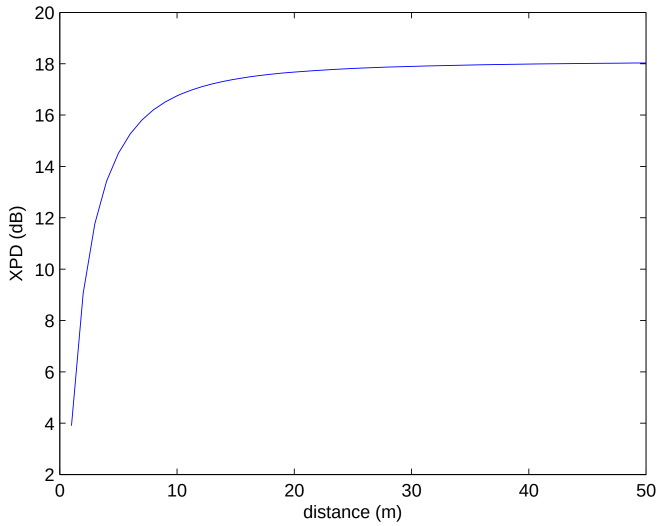

Figure 4.7: XPD versus distance, scenario 68

As seen from the graph, XPD increases with increasing distance.

XPD Behaviour of Channel Model where Scattering Parameters are Statistically Assigned

In order to study on XPD , we constituted a statistical model based on our channel model. We studied on first cycle of scenario 68. Using our model and Solution5-1, locations of scatterers are calculated. After that, normal directions, electrical properties and the orientations of discs are not calculated using formulas. Instead, they are assigned from statistical data. For this purpose, 444 cycles of scenario 68, each having an average number of 50 MPCs, are used. For each MPC, θ^i, θ^s, $\phi^s - \phi^i$ and ϵ_r are calculated and their histograms are obtained as :

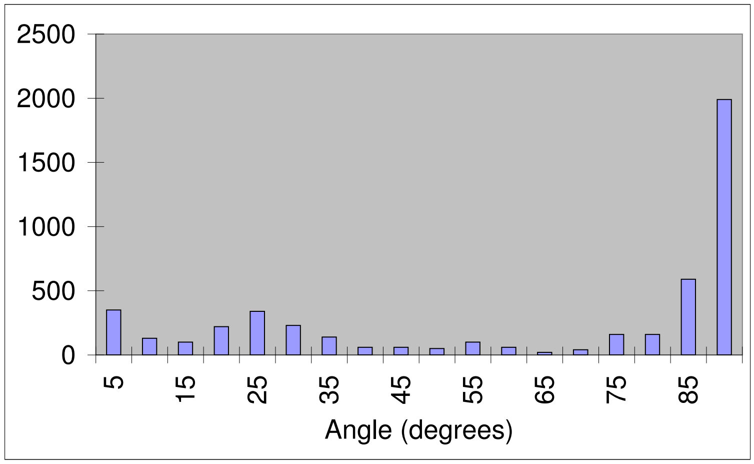

Figure 4.8: Histogram of θ^i obtained from measurement Data

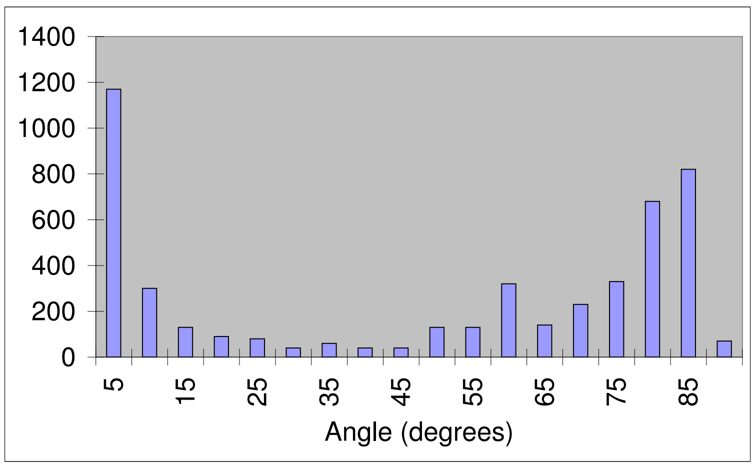

Figure 4.9: Histogram of the θ^s obtained from measurement Data

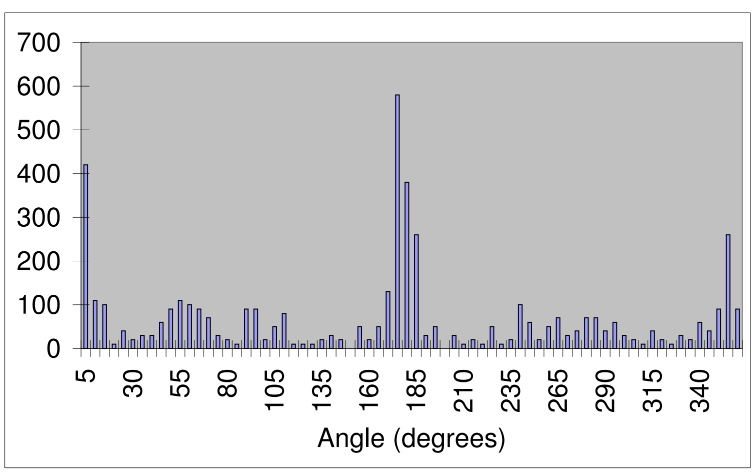

Figure 4.10: Histogram of the ϕ^s-ϕ^i obtained from measurement Data

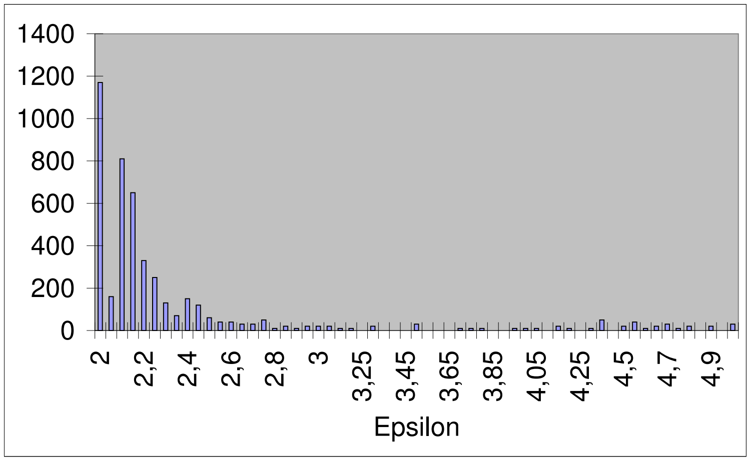

Figure 4.11: Histogram of the ϵ_r obtained from measurement Data

In order to assign parameters similar to the measurement data, data sequences similar to measurement based distributions are synthesized. They are shown below:

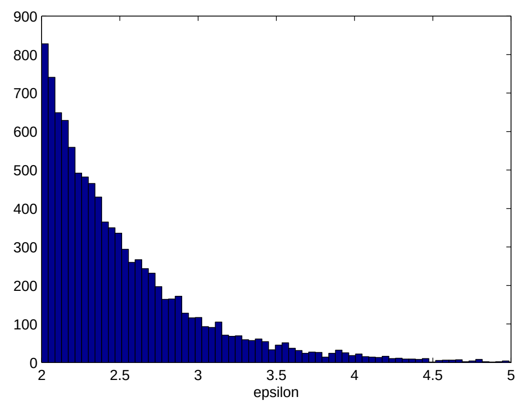

Figure 4.12: Synthesized histogram of the ϵ_r

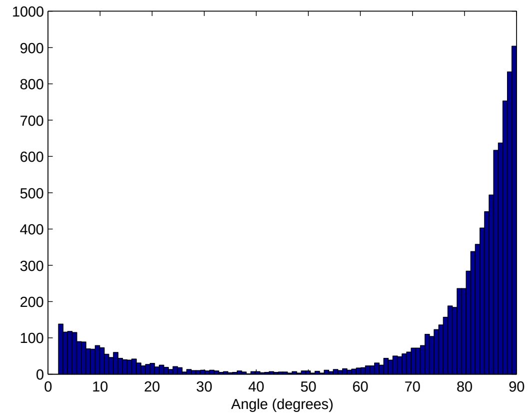

Figure 4.13: Synthesized histogram of the θ^i

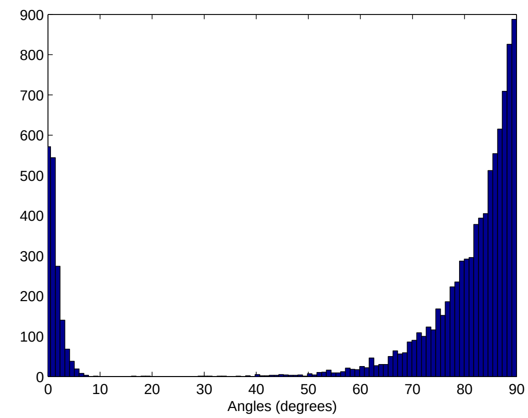

Figure 4.14: Synthesized histogram of the θ^s

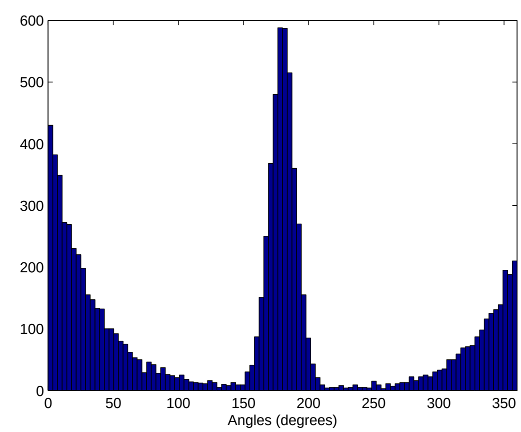

Figure 4.15: Synthesized histogram of the ϕ^s-ϕ^i

For each scatterer, parameters (θ^i, θ^s, $\phi^s - \phi^i$ and ϵ_r) are assigned using synthesized statistical distributions. Scattering coefficients are calculated using these parameters and Equations 3.63, 3.64, 3.65 and 3.66. Finally, XPD is calculated with these coefficients. Receiver location is changed gradually in the direction shown in Figure 4.6. For every new location of the receiver, scattering coefficient parameters are calculated using the geometrical relationship between TX, RX and the scatterer. Using these parameters, scattering coefficients are calculated using Equations 3.63, 3.64, 3.65 and 3.66. Finally, XPD ratio is calculated. The result is like:

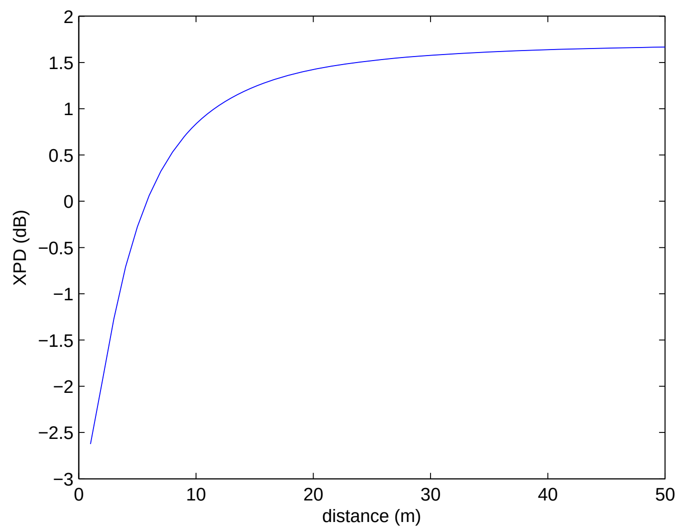

Figure 4.16: XPD versus distance, scenario 68

As seen from the graphs, XPD is increasing with increasing distance.

Chapter 5

Conclusions

In this thesis, a polarization included geometric channel model is developed. In order to get a realistic model, two indoor scenario measurements carried by Elektrobit Testing Corporation are studied: Scenario 68 and 72. Locations of scatterers are calculated using single bounce model estimation. There are five equations (Equations 3.1, 3.2, 3.3, 3.4 and 3.5) and three unknowns (X_s, Y_s, Z_s). Among combinations of five equations, Solution5-1 is found to be the most appropriate method for our model. So, Solution5-1 is used to find the locations. After that, synthetic scenarios adapted from real environments are constituted and used to decide on the multipaths to be used. Investigating the results of the synthetic scenarios gives us that seven percentage delay error is the criterion for the scatterers which can be modeled with single bounce model. 16 Scatterers for scenario 68 and 6 scatterers for scenario 72 are found within seven percentage delay error.

Discs are placed to those determined locations. Using physical optics and the vectorial relationship between incident and scattered field, electrical properties (ϵ_r) and orientations of discs (θ^x, θ^y, θ^z) are found. Calculated parameters of the environment for scenario 68 and 72 are shown in Tables 3.9 and 3.10, respectively. A detailed physical model is constructed for scenario 68 and 72.

Studying 444 cycles for scenario 68, statistical distributions are obtained for the parameters (θ^i, θ^s, $\phi^s - \phi^i$ and ϵ_r). They are shown in Figures 4.8, 4.9, 4.10 and 4.11. XPD characteristic of our model is discovered and compared with the results in [11]. For this purpose, scatterer locations are found in scenario 68. At those locations, parameters are assigned using statistical distributions and measurements. XPD is calculated for each changing distance. In addition to these, a 2D theoretical ray tracing model is constructed and its XPD characteristic is examined in the tunnel environment. All of the results are in accordance with each other; XPD increases with increasing distance [11].

Our model adds polarization properties and a geometric representation to the channel. It is a good tool to model the complex environments with a detailed description and can be used to analyze various characteristics of the environments.

Bibliography

[1] M. A. Jensen and J. W. Wallace, "A review of antennas and propagation for MIMO wireless communications," *IEEE Trans. Antennas Propagat.*, vol. 52, pp. 2810–2824, Nov. 2004.

[2] C. Oestges, V. Erceg, and A. J. Paulraj, "Propagation modeling of MIMO multipolarized fixed wireless channels," *IEEE Trans. Veh. Technol.*, vol. 53, pp. 644–654, May 2004.

[3] R. G. Vaughan, "Polarization diversity in mobile communications," *IEEE Trans. Veh. Technol.*, vol. 39, pp. 177–186, Aug. 1990.

[4] P. Kyritsi, D. C. Cox, R. A. Valenzuela, P. W. Wolniansky, "Effect of antenna polarization on the capacity of a multiple element system in an indoor environment," *IEEE J. Select. Areas Commun.*, vol. 20, pp. 1227–1239, Aug. 2002.

[5] C. Oestges, "Mutual information of non-kronecker structured dual-polarized 2X2 channels," *IEEE Trans. Veh. Technol.*, vol. 55, pp. 410–413, January 2006.

[6] W. Q. Malik, "Polarimetric characterization of ultrawideband propagation channels," *IEEE Trans. On Antennas and Propagation*, vol. 56, pp. 532–539, Feb. 2008.

[7] T. Swantesson, "A study of polarization diversity using an electromagnetic spatio-temporal channel model," *Vehicular Technology Conference 2000, 52nd*, vol. 1, pp. 79–86, 2000.

[8] T. Swantesson, "A physical MIMO radio channel model for multi-element multi-polarized antenna systems," *Vehicular Technology Conference 2001, 54th*, vol. 2, pp. 1083–1087, 2001.

[9] L. Hanlen, M. Fu, "Wireless communication systems with spatial diversity: A volumetric model," *IEEE Trans. On Wireless Communications.*, vol. 5, pp. 133–142, Jan. 2006.

[10] L. Jiang, L. Thiele, V. Jungnickel, "[11] L. Jiang, L. Thiele, V. Jungnickel, On the Modelling of Polarized MIMO Channel." *13th European Wireless Conference*, Paris, France, April 2007.

[11] M. Shafi, M. Zhang, A. L. Moustakas, P. J. Smith, A. F. Molisch, F. Tufvesson, and S. H. Simon, "Polarized MIMO channels in 3-D: Models, measurements and mutual information," *IEEE J. Select. Areas Commun.*, vol. 24, pp. 514–527, Mar. 2006.

[12] Elektrobit Corporation, "EB propsound CS radio channel sounder indoor campaign report",Finland, June 2005.

[13] B.H. Fleury, M. Tschudin, R. Heddergott, D. Dahlhaus and K.I. Pedersen, "Channel parameter estimation in mobile radio environments using the SAGE algorithm," *IEEE J. Select. Areas Commun.*, vol. 17, no. 3, pp. 434–450, March. 1999.

[14] Juan F. Valenzuela-Valdés, Miguel A. García-Fernández, Antonio M. Martínez-González, and David Sánchez-Hernández, "The role of polarization diversity for MIMO systems under Rayleigh-fading environments," *IEEE Antennas and Wireless Propagat.*, vol. 5, pp. 534–536, Nov. 2006.

[15] W.I. Stutzman, *Antenna Theory and Design.* John & Wiley Sons, Canada, 1981.

[16] D.A. McNamara, C.W.I. Pistorius, J.A.G. Malherbe, *Introduction to the Uniform Geometrical Theory of Diffraction.* Artech House, London, 1990.

[17] N.A. Albayrak, *RCS Computations with PO/PTD for Conducting and Impedance Objects Modeled as Large Flat Plates*, MS thesis, Bilkent University Dept. of Electrical and Electronics Engineering, Ankara, July 2005.

[18] T.C. Tu, C.M. Li, C.C. Chiu, "The performance of polarization diversity schemes in outdoor micro cells," *Progress in Electromagnetics research,PIER 55*, pp. 175–188, 2005.

[19] Jukka J.A. Lempiainen, J.K. Laiho-Steffens, "The performance of polarization diversity schemes at a base station in small/micro cells at 1800 MHz," *IEEE Trans. Veh. Technol.*, vol. 47, no. 3, pp. 1087–1092, August 1998.

[20] V. Soma, D.S. Baum, V. Erceg, R. Krishnamoorthy, A.J. Paulraj, "Analysis and modeling of Multiple-Input Multiple-Output (MIMO) radio channel based on outdoor measurements conducted at 2.5GHz for fixed BWA applications." *in Proc. IEEE ICC'2002 Conf.*, New York, April 2002.